

# Contents

<b>1</b>	<b>Theory</b>	<b>3</b>
1.1	Higgs Phenomenology . . . . .	3
<b>2</b>	<b>Neutral MSSM Higgs Search...</b>	<b>7</b>
2.1	The Search Strategy . . . . .	8
2.1.1	Motivation . . . . .	8
2.1.2	How to search for new phenomena? . . . . .	9
2.1.3	Signal Topology . . . . .	10
2.1.4	How to deal with Backgrounds . . . . .	13
2.1.5	Missing Mass Calculator . . . . .	14
2.2	Background Modeling and Validation . . . . .	16
2.2.1	Simulated Event Samples . . . . .	16
2.2.2	Top Quark Pair Production Validation . . . . .	18
2.2.3	Multi-jet Background . . . . .	19
2.2.4	$Z \rightarrow \tau\tau + \text{Jets}$ Background: Embedding Technique . . . . .	21
2.3	Systematic Uncertainties . . . . .	26
2.3.1	Detector-related Systematics Uncertainties . . . . .	26
2.3.2	$Z \rightarrow \tau\tau$ Embedding Systematics . . . . .	28
2.3.3	QCD Multi-Jet Systematics . . . . .	31
2.3.4	Theoretical Uncertainties . . . . .	35
2.4	Results . . . . .	36
2.4.1	LHC Procedure For Limits Setting . . . . .	36
2.4.2	Exclusion Limits . . . . .	38
2.4.3	Summary . . . . .	39
.1	Object Reconstruction, Preselection and Efficiency Corrections . . .	46
.1.1	Electrons . . . . .	46
.1.2	Muons . . . . .	47
.1.3	Jets . . . . .	48
.1.4	b-Tagging . . . . .	48
.1.5	Taus . . . . .	48
.1.6	Overlap Removal . . . . .	48
.1.7	Missing Transverse Energy . . . . .	49
.1.8	Vertices . . . . .	49
.1.9	Event Cleaning . . . . .	49
.1.10	Monte Carlo Corrections . . . . .	50



# Chapter 1

## Theory

### 1.1 Higgs Phenomenology

The Higgs sector of the Minimal Supersymmetric Standard Model (MSSM) consists of two SU (2) doublets,  $H_1$  and  $H_2$ , whose relative contribution to electroweak symmetry breaking is determined by the ratio of vacuum expectation values of their neutral components,  $\tan \beta = v_2 / v_1$ . The spectrum of physical Higgs bosons is richer than in the SM, consisting of two neutral scalars  $h$  and  $H$ , one neutral pseudoscalar,  $A$ , and two charged scalars,  $H^\pm$ . At the tree level, the mass matrix for the neutral scalars can be expressed in terms of the parameters  $M_Z$ ,  $M_A$  and  $\tan \beta$ , and the mass of the lightest scalar  $h$  is bounded from above by  $M_Z$ . However, radiative corrections – especially those involving top and bottom quarks and their supersymmetric partners, the stop and sbottom squarks – can significantly alter the tree-level predictions for the Higgs-boson masses, and bring along a dependence on a large number of free parameters of the MSSM. While the CP symmetry is conserved at tree level in the MSSM Higgs sector, radiative corrections can also introduce CP-violating phases, and induce mixing among all three neutral states. In this report, however, we will focus on the CP-conserving case, by considering only real values for the parameters in the soft SUSY-breaking Lagrangian and for the Higgs mass in the superpotential. In general, the couplings of the MSSM Higgs bosons to gauge bosons and matter fermions differ from those of the SM Higgs. However, in large regions of the MSSM parameter space one of the scalars has SM-like couplings, while the other Higgs bosons are decoupled from the gauge bosons, and their couplings to down-type (up-type) fermions are enhanced (suppressed) by  $\tan \beta$ . As in the SM, gluon fusion is one of the most important production mechanisms for the neutral Higgs bosons, whose couplings to the gluons are mediated by the top and bottom quarks and their superpartners. However, for intermediate to large values of  $\tan \beta$  the associated production with bottom quarks can become the dominant production mechanism for the neutral Higgs bosons that have enhanced couplings to down-type fermions. The production of the charged Higgs  $H^\pm$ , on the other hand, proceeds mainly through its coupling to a top-bottom pair. A sufficiently light  $H^\pm$  is produced in the decay of a top quark, and it decays dominantly in a tau-neutrino pair. A heavy  $H^\pm$  is produced in association with a top quark and it decays dominantly in a top-bottom pair. The discovery by ATLAS and CMS of

what appears to be a neutral scalar with mass around 125.5 GeV [1, 2] puts the studies of the Higgs sector of the MSSM in an entirely new perspective. In order to remain viable, a point in the MSSM parameter space must now not only pass all the (ever stricter) experimental bounds on superparticle masses, but also lead to the prediction of a scalar with mass, production cross section and decay rates compatible with those measured at the LHC. In particular, the relatively large mass of the roughly-SM-like scalar discovered at the LHC implies either very heavy stops, of the order of 3 TeV, or a large value of the left-right stop mixing term (see, e.g., Refs. [648,649]). The benchmark scenarios routinely considered in MSSM studies had been devised when the Higgs sector was constrained only by the LEP searches, and many of them, such as the so-called no-mixing scenario, are now ruled out because they predict a too-light SM-like scalar. Others, such as the so-called mmax scenario, are constrained for the opposite reason, i.e. they can predict a too-heavy SM-like scalar. To address the need for new benchmark scenarios to be used in future studies of the MSSM Higgs sector, in Section 14.2 we will define scenarios that are compatible both with the properties of the Higgs boson discovered at the LHC and with the current bounds on superparticle masses. The fact that information on the Higgs boson mass, production and decays has now become available also puts new emphasis on the need for accurate theoretical predictions of those quantities. In the studies presented in this report, the masses and mixing of the MSSM Higgs bosons are computed with the public code F EYN H IGGS [2427], which implements the full one-loop radiative corrections together with the dominant two-loop effects. The theoretical accuracy of the prediction of F EYN H IGGS for the

lightest-scalar mass was estimated to be of the order of 3 GeV [26, 650, 651], i.e., already comparable to the accuracy of the mass measurement at the LHC. Improving the accuracy of the theoretical prediction for the MSSM Higgs masses will require the inclusion in public computer codes of the remaining two-loop effects [652654] and at least the dominant three-loop effects [655657]. The production and decay rates of a SM-like Higgs boson in the MSSM are sensitive to contributions from virtual SUSY particles, and their measurement at the LHC combined with the searches for additional Higgs bosons can be used to constrain the MSSM parameter space. To this effect, the theoretical predictions for cross section and decays must include precise computations of the SUSY contributions. In Section 14.3 we use the public code S US H I [641] and the POWHEG implementation of Ref. [77] to compute the total and differential cross sections for neutral Higgs-boson production in gluon fusion, including a NLO-QCD calculation of quark and squark contributions plus higher-order quark contributions adapted from the SM calculation. We show that the SUSY contributions can be sizeable in regions of the MSSM parameter space where the third-generation squarks are relatively light, and discuss the theoretical uncertainty of the predictions for the cross sections. Finally, we study and update the exclusion limits on light charged MSSM Higgs bosons in the  $(M_H, \tan \beta)$ -plane in various benchmark scenarios in Section 14.4. Particular emphasis is placed on the dependence of the limits on the variation of SUSY parameters. We also provide improved NLO-QCD cross section predictions for heavy charged Higgs production in the so-called four and five-flavor schemes in Section 14.5. The five-flavor scheme cross section is calculated with a new scheme

for setting the factorization scale and takes into account the theoretical uncertainty from scale variation and the PDF,  $s$  and bottom-mass error. We observe good agreement between the 4FS and 5FS NLO-calculations and provide a combined prediction following the Santander matching.

### 14.2 New MSSM benchmark scenarios

Within the MSSM an obvious possibility is to interpret the new state at about 125.5 GeV as the light CP-even Higgs boson [334, 338, 648, 649, 658, 662]. At the same time, the search for the other Higgs bosons has continued. The non-observation of any additional state in the other Higgs search channels puts by now stringent constraints on the MSSM parameter space, in particular on the values of the tree-level parameters  $M_A$  (or  $M_H$ ) and  $\tan\beta$ . Similarly, the non-observation of supersymmetric (SUSY) particles puts relevant constraints on the masses of the first and second generation scalar quarks and the gluino, and to lesser degree on the stop and sbottom masses (see Refs. [663, 664] for a recent summary). Due to the large number of free parameters, a complete scan of the MSSM parameter space is impractical in experimental analyses and phenomenological studies. Therefore, the Higgs search results at LEP were interpreted [458] in several benchmark scenarios [16, 665]. In these scenarios only the two parameters that enter the Higgs sector tree-level predictions,  $M_A$  and  $\tan\beta$ , are varied (and the results are usually displayed in the  $M_A$ – $\tan\beta$  plane), whereas the other SUSY parameters, entering via radiative corrections, are fixed to particular benchmark values which are chosen to exhibit certain features of the MSSM Higgs phenomenology. These scenarios were also employed for the MSSM Higgs searches at the Tevatron and at the LHC. By now, most of the parameter space of the original benchmark scenarios [16, 665] has been ruled out by the requirement that one of the CP-even Higgs boson masses should be around 125.5 GeV. Consequently, new scenarios have been proposed [31], which are defined such that over large parts of their available parameter space the observed signal at about 125.5 GeV can be interpreted in terms of one of the (neutral) Higgs bosons, while the scenarios exhibit interesting phenomenology for the MSSM Higgs sector. The benchmark scenarios are all specified using low-energy MSSM parameters, i.e. no particular soft SUSY-breaking scenario was assumed. Constraints from direct searches for Higgs bosons are taken into account, whereas indirect constraints from requiring the correct cold dark matter density,  $\text{BR}(b \rightarrow s)$ ,  $\text{BR}(B_s \rightarrow \mu^+ \mu^-)$  or  $(g-2)$  are neglected. However interesting, those constraints de



## Chapter 2

# The Search for neutral MSSM Higgs Bosons in the final state:

$$\tau^+ \tau^- \rightarrow e\mu + 4\nu$$

This chapter contains the main work of this thesis, reports about the search for the neutral MSSM Higgs boson decaying in tau pairs and fully leptonic final state. This search is based on 2012 8 TeV data recorded by ATLAS experiment at Large Hadron Collider.

Discovering the mechanism responsible for electroweak symmetry-breaking and the origin of mass for elementary particles has been one of the major goals of the physics program at the Large Hadron Collider (LHC) [1]. In the Standard Model (SM) this mechanism requires the existence of a single scalar particle, the Higgs boson [2, 3, 4, 5, 6]. In the Minimal Supersymmetric extension of the Standard Model (MSSM) [7, 8] the Higgs sector is composed of two Higgs doublets of opposite hyper-charge, resulting in five observable Higgs bosons. Two of these Higgs bosons are neutral and  $CP$ -even ( $h, H$ ), one is neutral and  $CP$ -odd ( $A$ ) and two are charged ( $H^\pm$ ). At tree level their properties such as masses, widths and branching ratios can be predicted in terms of only two parameters, often chosen to be the mass of the  $CP$ -odd Higgs boson  $m_A$ , and the ratio of the vacuum expectation values of the two Higgs doublets  $\tan\beta$  (more detail in chapter ??).

This chapter is divided in three sections: in section 2.1 an introduction to experimental searches and to the strategy of this particular analysis is given, in section ?? is described the core of this thesis work, i.e. the detail of the background modeling for this analysis, while in section ?? the result of the search are presented.

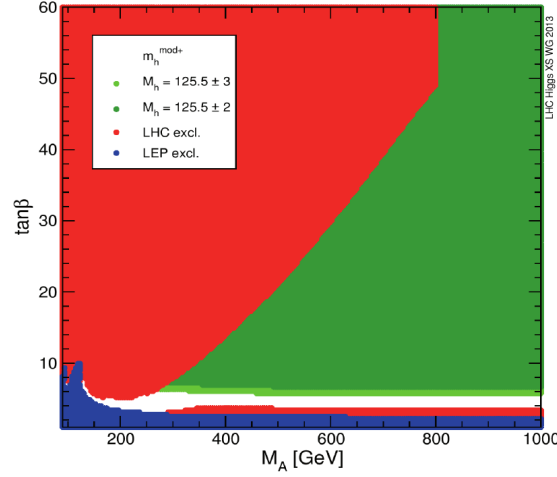


Figure 2.1:  $m_A - \tan\beta$  plane for the  $m_h^{mod+}$  scenario, with excluded region from direct Higgs searches at Lep (blue) and LHC (red). The two green shades corresponds to the allowed parameter space for the assumption of  $M_h = 125.5 \pm 2(3)$  GeV. For more detail see [1].

## 2.1 The Search Strategy

### 2.1.1 Motivation

Under the light of the recent discovery of a Higgs boson with mass of 125 GeV [1], remains an open question whether this new particle constitutes all the pieces of the Higgs sector or if it is only one of several bosons predicted in some theories that go beyond the SM. The most recent measurements [2] of its properties shows it to be, within experimental uncertainties, perfectly compatible with the SM Higgs boson, however such a new particle can be accommodated within several beyond the standard model (BSM) theories, this is particularly true for Super Symmetry.

There are two approaches to explore the Higgs sector: studying the coupling of the Higgs boson with vector bosons and fermions, given the unitarity property of scattering amplitudes for longitudinal vectors and fermions, one can understand if this particle is fully responsible for the generation of the masses of all the other SM particles. Another approach is to directly search for additional Higgses in a well defined model. In this thesis the last approach is followed, new particles are sought within the MSSM scenario (see chapter ??).

In the MSSM a Higgs boson with properties that resembles the one for a SM Higgs boson occurs naturally in large regions of parameter space, for practical reasons however, it is useful to fix parameters of the model to achieve what is called a benchmark scenario. With the recent discovery, benchmark scenarios of the MSSM have been updated to fit with the new constraints (more details on benchmark scenarios are in chapter ??), as an example in figure ?? are reported the current exclusion limits for one of those updated scenarios,  $m_h^{mod+}$ , the green area represents what is currently allowed in the  $m_A - \tan\beta$  plane showing that there is still plenty of room for BSM Higgses.



### 2.1.2 How to search for new phenomena?

Typically new physics searches are looking for a signal that is additive on top of the background, an observation of an excess or exclusion of a signal is then characterized by statistical statements. A *statistical test* is a rule used to reject or accept an hypothesis. An hypothesis is a statement about the distribution of the data. In the search for new phenomena at the LHC frequentist statistical tests are used [?], where two hypotheses are compared: the background only hypothesis  $H_0$ , which plays the role of the null hypothesis, and the signal plus background hypothesis  $H_1$ , which is the alternative. In this section an introduction to LHC statistical procedure is given, for more details see section ??.

In a search for new physics usually a *signal region* is defined in data where events are counted, the number of observed events  $N_{SR}$  is a random variable described by a Poisson distribution, in case the null hypothesis is true  $\nu_B$  events are expected, while  $\nu_B + \nu_S$  are expected for the  $H_1$  alternative hypothesis, the probability model for null and the alternate hypothesis is then respectively  $\text{Pois}(N_{SR}|\nu_B)$  and  $\text{Pois}(N_{SR}|\nu_B + \nu_S)$ . The evidence for a signal shows up as an excess of events, a way to quantify the compatibility of the null hypothesis with data is to make a *significance* test, this leads to the calculation of the probability that the background-only would produce at least as many as the observed events, this is the so called p-value, which in this case is expressed by the formula:

$$\text{p-value} = \sum_{n=N_{SR}}^{\infty} \text{Pois}(n|\nu_B)$$

Calculating p-value is a way to characterize an excess, in high energy physics the commonly accepted p-value that qualifies as discovery is  $2.87 \times 10^{-7}$ , which translated to the probability of a gaussian distribution correspond to five standard deviation.

In case no excess is observed, the procedure is to build a statistical test where the null hypothesis is accepted and at the same time the signal hypothesis is rejected with a fixed predetermined probability, called confidence level. A statistical test is a rule that defines a region in the space of data for which a given hypothesis can be accepted or rejected, often rather than using a full set of data  $\mathcal{D}$ , it is convenient to define a *test statistic*,  $T$ , which is usually a single number computed from the data, the two hypothesis implies different distributions for  $T$ , then one defines an acceptance region  $W$  in terms of the test statistic, if  $T \in W$  the  $H_0$  is rejected and  $H_1$  accepted and vice versa, the probability with which one rejects  $H_1$  or  $H_0$  is then given by the choice of  $W$  and  $T$ . Neuman and Person provided a framework for hypothesis testing that addresses the choice of the test statistic [?].

A discriminating variable is often used to help separating signal and backgrounds, this can be any of the observables of the experiment, a usually chosen observable is for example the invariant mass of final state particles, knowing the probability density function  $f(x)$  for this observable for the two hypothesis one can complete the above mentioned statistical model with what is called a marked Pois-

son for a set of data  $\mathcal{D}$ :

$$\text{Pois}(N_{SR}|\nu) \prod_{i \in \mathcal{D}}^{N_{SR}} f(x_i|\vec{\theta})$$

here is made explicit that  $f(x)$  depends also on a set of additional parameter  $\vec{\theta}$ , called nuisance parameter, those embed effects like detector mismodeling or theoretical uncertainty. With the use of a discriminating variable one can take advantage of additional information to disentangle between signal and backgrounds.

Summarizing, there are several ingredients that constitute a search for new physics and will be discussed with more details in the following sections:

- Define a signal region in data where signal is enhanced with respect to the backgrounds, detailed in section ??
- Define a discriminating variable which is usefull to disentangle between signal and backgrounds, section ??
- Define the probability model, i.e., the expectation for the distribution of the discriminating variable for signal and background hypotesis, this is one of the most importat point of a search and main part of the work of this thesis, detailed in section ??
- Define a test statistics, which is detailed for the LHC in section ??.

### 2.1.3 Signal Topology

This section describes the strategy to enhance the search sensitivity taking advantage of the signal topology. The Sensitivity of a search is the signal strenght that is expected to be excluded in case of no signal. If one is searching for a rare process, then the analysis strategy, i.e. the plan or the steps to enhance the signal sensitivity of the search, is crucial. A further consideration is that this search is complementary to the Standard Model Higgs search in tau final state, the focus is then on non explored phase space from SM.

In the MSSM for large region of parameter space one found that one of the  $CP$ -even neutral Higgses is has properties that resemble the one of the SM Higgs, this is usually the case for the lightest Higgs,  $h$ , the other two,  $H$  and  $A$ , thend to be degenerate in mass and decouple from gauge bosons. An interesting fenomenological point is that the coupling of the latter two Higgses with down (up) type fermions are enhanced (suppressed) by  $\tan \beta$ , meaning that for large  $\tan \beta$  bottom-quark and  $\tau$  lepton will play a more important role than in the SM case either for production and decay.

The production of the neutral  $CP$ -even MSSM Higgs bosons at hadron colliders proceeds via the same processes as for the SM Higgs production. However, the pseudoscalar  $A$  instead cannot be produced in association with gauge bosons or in vector boson fusion (VBF) at tree-level, as this coupling is forbidden due to  $CP$ -invariance. At the LHC one of the most relevant production mechanisms for the MSSM Higgs bosons is gluon-gluon fusion,  $gg \rightarrow A/H/h$ . In addition, the

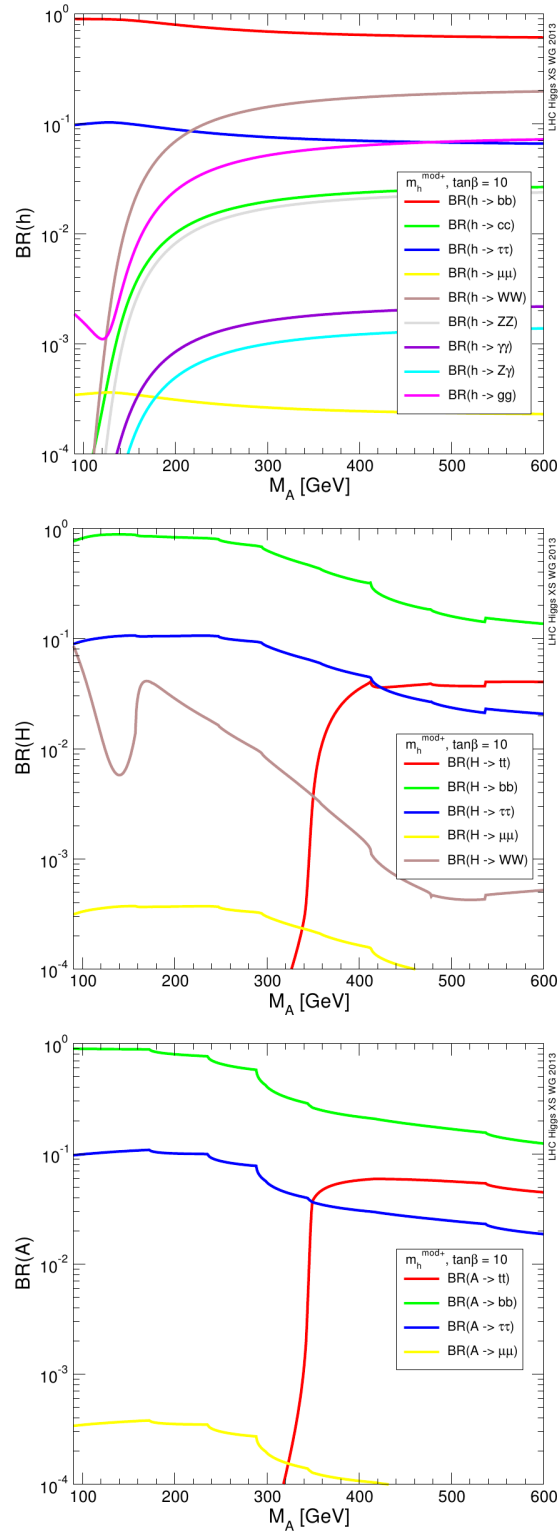


Figure 2.2: Branching fraction for the MSSM neutral higgses in the bla scenario.

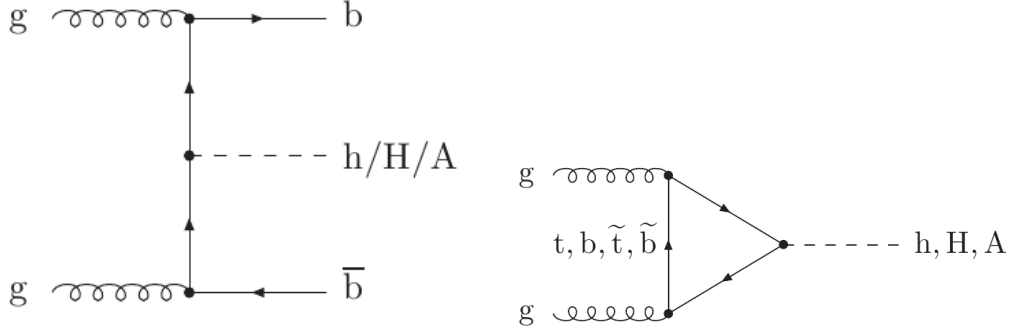


Figure 2.3: Diagram for b-associated production and gluon-gluon fusion for MSSM neutral Higgs.

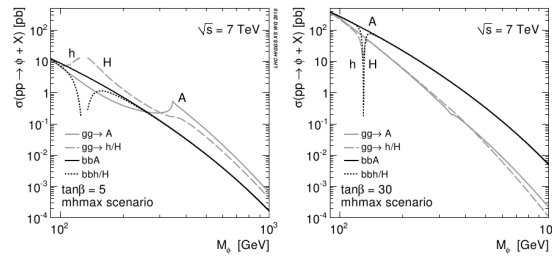


Figure 2.4: Cross section for different MSSM neutral Higgs production mode.

production in association with  $b$ -quarks becomes important for large value of  $\tan \beta$ . Those are the two production mechanism that are considered in this analysis, figure ?? shows the feynman-diagram for those processes. The search is divided in two category which are optimized for the two different production mode considered, in the gluon-fusion category is required a b-jet veto, in fact no b-jet in the final state are present for this production mode. In contrast a b-jet tag is required for b-associated production, this category is expected to be very sensitive to  $\tan \beta$ . The two category are ortogonal and present different backgrounds contributions, which can be optimized separately.

The decays of the neutral MSSM Higgs bosons (in the assumption that all supersymmetric particle are heavy enough) are the same as for the SM one with the already cited exception of  $A$ . Figure ?? shows the decay branching fractions for  $H$  and  $A$ , as a function of the mass and for  $\tan \beta =$ , the decay into tau pair is the most important after  $b\bar{b}$ . The decay channel in  $b\bar{b}$  is challenging due to the huge background from QCD multi-jet, in this analysis the decay in tau pairs is choosen. In this thesis only cases in which the taus decay one in  $e + 2\nu$  and the other in  $\mu + 2\nu$  are considered, This final state corresponds to a total  $\tau^+\tau^-$  branching ratio of approximately 6%.

Summarising, the signal topology is characterised by a final state with an electron, a muon, and missing transverse energy due to the presence of four neutrinos from the  $\tau$  decays. Furthermore, the final state may be split by the presence or absence of a  $b$ -quark initiated jet, depending on the production process. This signature is achieved experimentally by requiring: an OR of a single electron and an electron-muon trigger, exactly one reconstructed electron and one muon in the final state, the two leptons should be of opposite charge and isolated. With isolation it's meant that in a cone around the lepton there should be little energy deposit (should not be sorraunded by other particle, common of non-prompt leptons coming from jets). More detail about isolation properties are detailed in section ???. Full detail on actual preselections regarding all the quality requirements on object reconstruction are reported in appendix ??.

### 2.1.4 How to deal with Backgrounds

The signal topology described in the previous section common to many other processes, unfortunately those have higher cross section than the signal we are looking for, a set of additional selection has been studied to enhance the sensitivity of the search, or in other words, to increase the signal to background ratio. The most important backgrounds to this search are the production of  $Z \rightarrow \tau\tau$  + jets, the top quark ( $t\bar{t}$  and single top production is intended), diboson production (like  $WW$  or  $ZZ$  events) and events with non-prompt leptons coming from QCD multi-jet (in short QCD multi-jet). Vector bosons production like  $W \rightarrow l\nu$  or  $Z \rightarrow ll$  + jets (with  $l$  here meanung either  $e$  or  $\mu$ ) are also considered, however those processes have a limited impact.

The final state of Higgs decaying into tau pair coincide with the one from  $Z \rightarrow \tau\tau$  process, this is then an irreducible background, however exploiting the different kinematics of the Higgs decay and the other backgrounds it possible to distinguish

between signal and them. The most striking is that the higgs (like  $Z \rightarrow \tau\tau$ ) selecting an electron and one muon coming from the tau decay, due to the high mass the taus will be back to back and their decay products will be highly boosted, this gives rise to two features: the mu-e will be more likely back to back, as you can see in figure 2.5 that shows the angle between the leptons in the transverse plane  $\Delta\phi = |\phi_e - \phi_\mu|$ <sup>1</sup> prefer configuration in which the leptons are in opposite hemisphere. Furthermore the neutrinos will be more likely collinear with the leptons (given the high boost the taus receive from Higgs decay). This feature can be mathematically seen as the sum of scalar product between missing energy and the leptons four-vectors in the transverse plane, if the vectors are normalised to unit vectors then what remains is a relation only between angles:

$$\hat{E}_T^{miss} \cdot (\hat{P}_T^\mu + \hat{P}_T^e) = \cos(\Delta\phi_{E_T,\mu}) + \cos(\Delta\phi_{E_T,e})$$

In the assumption of collinearity and of leptons back-to-back that scalar product is equal to zero, in fact it would be equal to zero for each of the neutrinos being it collinear with one lepton and back-to-back with the other. As can be seen from figure 2.5 in fact the distribution of that variable has its more likely values at zero. These two features can be used to distinguish between mu-e coming from decay from highly boosted object and the one coming from W decays in top or in dibosons backgrounds which will have a more spread distribution. In b-veto category these two selections are sufficient to suppress contribution from dibosons, no other selection is applied in this category because it has been shown to not bring significant improvement.

In the b-tag category the situation is different, the request of b-jet enhance backgrounds with high jet activity as top production, given the relatively low jet activity of our Higgs events (also in the case of b-associated production) it's possible to separate them from top production which instead is very likely to have 2 or more highly energetic jets in the event, requesting a small jet activity, this is achieved by requesting the sum of the jets transverse momentum to be small, we call this variable  $H_T$ . Another feature that distinguishes top pair production from Higgs is the much higher invariant mass of the former final state, in the transverse plane all the leptons will tend to have a higher momentum, we then use the sum of lepton  $p_t$  and  $E_T^{miss}$  as a discriminating variable, requesting it to be small. Figure ?? shows the distribution of these two variables after the request of a b-jet.

Plots with MMC mass as a function of selection that shows how effective they are in reducing backgrounds.

In table ?? a summary of all the selection variables used with their optimized cut values is reported. While in table ?? the number of events that survives at each cut stage for different background is reported.

### 2.1.5 Missing Mass Calculator

Accurate invariant mass reconstruction of a di-tau system is a challenging task due to the escaping neutrinos. In this analysis, with four neutrinos in the final state,

---

<sup>1</sup>This is actually more complicated: one has to take care of the sign of  $\phi$  see chapter ??

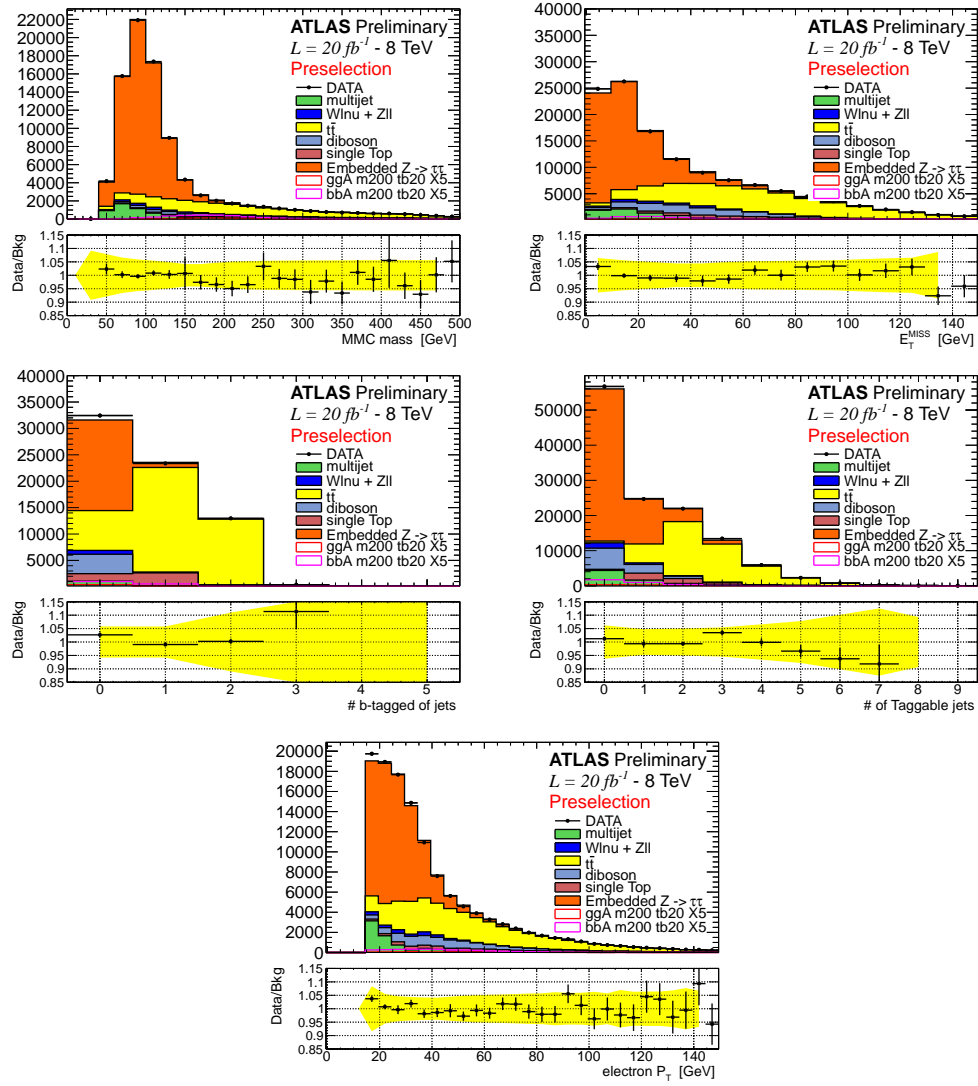


Figure 2.5: bla

the number of unknown largely exceed the number of constraints, several approximation are possible to further constraint the neutrinos, for example assuming them collinear to the other leptons from tau decay, however those approximation suffers of limitations.

In this analysis we use the so called missing mass calculator (MMC) [55] technique for the calculation of the di-tau system invariant mass. This technique employs additional information from the well known tau decay to constraint the system, this is achieved by minimising a likelihood function defined in the kinematically allowed phase space region, the result is a more precise measurement of the di-tau system invariant mass and a considerable improvement in resolution. The invariant mass distribution calculated with the MMC technique is referred in the following as  $MMC_{mass}$  and is used as discriminating variable in the limits setting.

## 2.2 Background Modeling and Validation

This section describes the strategies for background modeling and validation. Monte Carlo (MC) simulation is extensively used for model either background and signal, in section 2.2.1 a brief description of the simulated sample used is given.

Monte Carlo (MC) Simulation of the background and signal processes is extensively used that are used to model the backgrounds are described in section ???. Monte Carlo simulations of any process are usually prone to systematic uncertainties due to non-perfect descriptions of pileup effects, underlying event and detector performance, therefore, data-driven background estimation method are employed for describe  $Z \rightarrow \tau\tau$  and QCD multijet backgrounds, described respectively in section ?? and ??. Other background processes, such as  $t\bar{t}$ , single top, dibosons,  $Z \rightarrow ll + \text{jets}$  (where  $l = e, \mu$ ) and  $W + \text{jets}$ , are estimated using MC predictions. Given the particular importance of  $t\bar{t}$  a dedicated study to validate this background has been made and described in section ??.

In this section we make use of analysis tools and object definition (like electrons, jet or muon) described in chapter ??. Furthermore a set corrections is applied to simulated events to take into the non perfect description of detector performance and response, full detail on those corrections is reported in appendix ??. Systematic uncertainties on the background model predictions are detailed in Section 2.3.

### 2.2.1 Simulated Event Samples

The generators used for the different processes are described below.

Signal production via the gluon fusion process,  $gg \rightarrow A/H/h$ , was simulated with POWHEG [30] and the associated  $b\bar{b}A/H/h$  production with SHERPA [31]. The pseudoscalar Higgs boson samples were generated in the mass range from 90 GeV to 400 GeV and 90 GeV to 300 GeV for  $ggH$  and  $b\bar{b}A$  production, respectively, and at  $\tan\beta = 20$ . The same kinematics are assumed for  $A/h/H$  Higgs bosons decay products and at other  $\tan\beta$  values. Appropriate reweighting is applied according to the different cross-sections. The  $m_h^{\text{max}}$  MSSM benchmark scenario [34] is assumed.



Table 2.1: The cross sections (multiplied by the relevant branching ratios (BR)) used in this note. Signal cross sections are shown for  $m_A = 150$  GeV and  $\tan \beta = 20$

Process	Cross-section (pb) [ $\times$ BR]
$W \rightarrow \ell + \text{jets}$ ( $\ell = e, \mu, \tau$ )	$12.22 \times 10^3$
$Z/\gamma^* \rightarrow \ell\ell + \text{jets}$ ( $m_{\ell\ell} > 60$ GeV)	$1.15 \times 10^3$
$Z/\gamma^* \rightarrow \ell\ell + \text{jets}$ ( $10 < m_{\ell\ell} < 60$ GeV)	$4.35 \times 10^3$
$t\bar{t}$	137.3
Single top $t$ -, $s$ - and $Wt$ -channels	28.4, 1.8, 22.4
Diboson WW, WZ and ZZ	20.6, 6.8, 1.55
Signal ( $m_A = 150$ GeV, $\tan \beta = 20$ , $m_h^{max}$ scenario)	
$gg \rightarrow A \times \text{BR}(A \rightarrow \tau\tau) \times \text{BR}(\tau\tau \rightarrow e\mu + 4\nu)$	$16.8 \times 0.118 \times 0.062$
$gg \rightarrow H \times \text{BR}(H \rightarrow \tau\tau) \times \text{BR}(\tau\tau \rightarrow e\mu + 4\nu)$ ( $m_H = 151$ GeV)	$18.4 \times 0.119 \times 0.062$
$gg \rightarrow h \times \text{BR}(h \rightarrow \tau\tau) \times \text{BR}(\tau\tau \rightarrow e\mu + 4\nu)$ ( $m_h = 129$ GeV)	$13.7 \times 0.110 \times 0.062$
$b\bar{b}A \times \text{BR}(A \rightarrow \tau\tau) \times \text{BR}(\tau\tau \rightarrow e\mu + 4\nu)$	$39.4 \times 0.118 \times 0.062$
$b\bar{b}H \times \text{BR}(H \rightarrow \tau\tau) \times \text{BR}(\tau\tau \rightarrow e\mu + 4\nu)$ ( $m_H = 151$ GeV)	$35.7 \times 0.119 \times 0.062$
$b\bar{b}h \times \text{BR}(h \rightarrow \tau\tau) \times \text{BR}(\tau\tau \rightarrow e\mu + 4\nu)$ ( $m_h = 129$ GeV)	$4.71 \times 0.110 \times 0.062$

The production of  $W$  and  $Z/\gamma^*$  bosons in association with jets was simulated with the ALPGEN [23] generator. The  $t\bar{t}$  process was generated using the POWHEG generator. The single-top (s-channel,  $Wt$ ) processes were generated using MC@NLO [25], while single-top (t-channel) processes were generated with AcerMC [26]. The production of diboson ( $WW$ ,  $WZ$ ,  $ZZ$ ) were generated with HERWIG [27]. For all ALPGEN and MC@NLO samples described above, the parton shower and hadronisation were simulated with HERWIG and the activity of the underlying event with JIMMY [28]. Different parton density functions (PDFs) sets are used depending on the generator - CTEQ6L1 [32] is used by ALPGEN and AcerMC while CT10 [33] is used by SHERPA, POWHEG and MC@NLO.

The cross-sections of the MC event samples used in this note are summarised in Table 2.1. The  $W/Z + \text{jets}$  and  $b\bar{b}A/H/h \rightarrow \tau\tau$  cross sections are calculated to NNLO. Those for  $t\bar{t}$  comes from direct cross section measurement []. The single top and diboson cross sections are calculated at NLO for single top and dibosons. Finally, the direct  $gg \rightarrow A/H/h \rightarrow \tau\tau$  signal cross sections are calculated at NNLO and NLO for the top loop and the bottom loop and top/bottom loops interference, respectively.

TAUOLA [36] and PHOTOS [37] are used to model the tau lepton decay and additional photon radiation from charged leptons in the leading-log approximation, respectively, except for SHERPA samples.

All MC event samples were passed through the full simulation of the ATLAS detector using GEANT4 [38, 39]. The effects of the simultaneous recording of several events from the same or neighbouring bunch crossings (pile-up) are considered in the simulation.

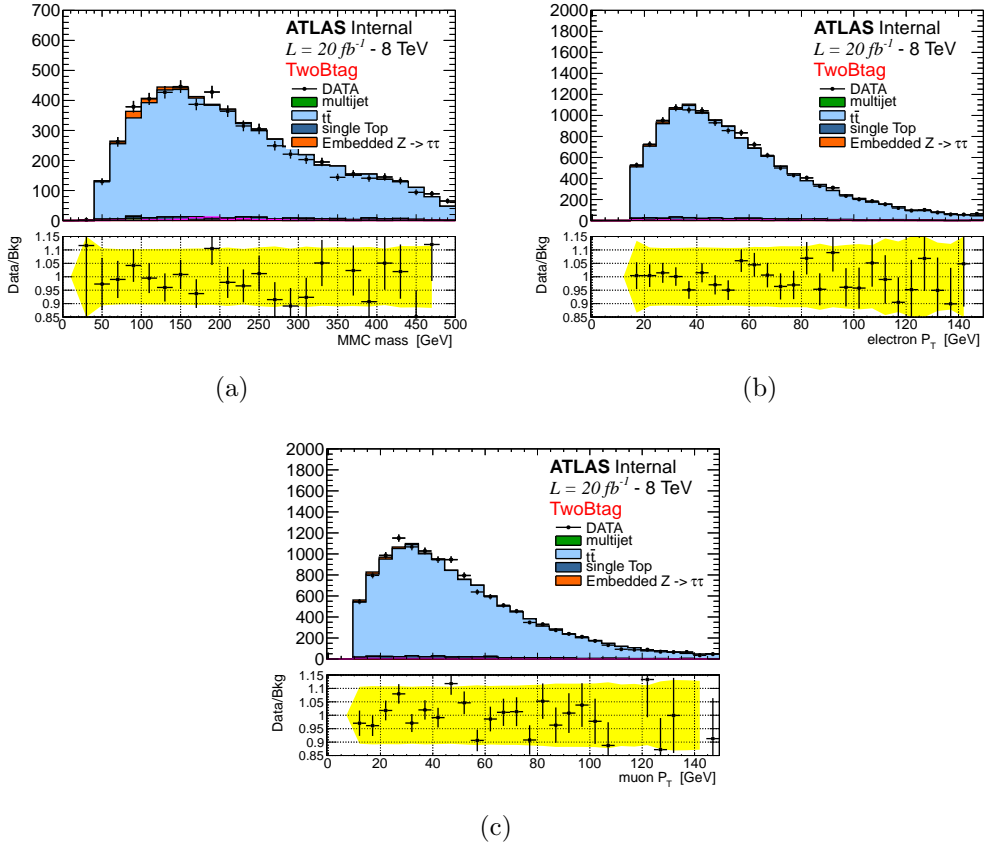


Figure 2.6: Distributions of a) the MMC mass, b) the transverse momentum of the electron  $p_t(e)$  and c) the transverse momentum of the muon  $p_t(\mu)$ , for both data and MC in the  $t\bar{t}$  control region. The uncertainties on the points for the ratio plot show the statistical uncertainty on the data to background ratio, whereas the yellow band show the total systematic uncertainty on this ratio.

### 2.2.2 Top Quark Pair Production Validation

The background from top quark pair production is estimated using a sample of events from the POWHEG-PYTHIA MC generator. To validate this MC sample, a  $t\bar{t}$  rich control region is defined using events passing the preselection described in section ?? with the additional requirement of two b-tagged jets. Figures 2.6 and 2.7 show a set of kinematic and analysis selection variables in this CR, for both data and the MC prediction, good agreement between data and the background model is found. Also the prediction of the event yield in this CR is in good agreement with data: an overall data to background ratio of  $0.998 \pm 0.011(\text{stat.}) \pm 0.110(\text{sys.})$  is observed. The total systematic uncertainty on the ratio is dominated by the uncertainty on the b-tagging efficiency.

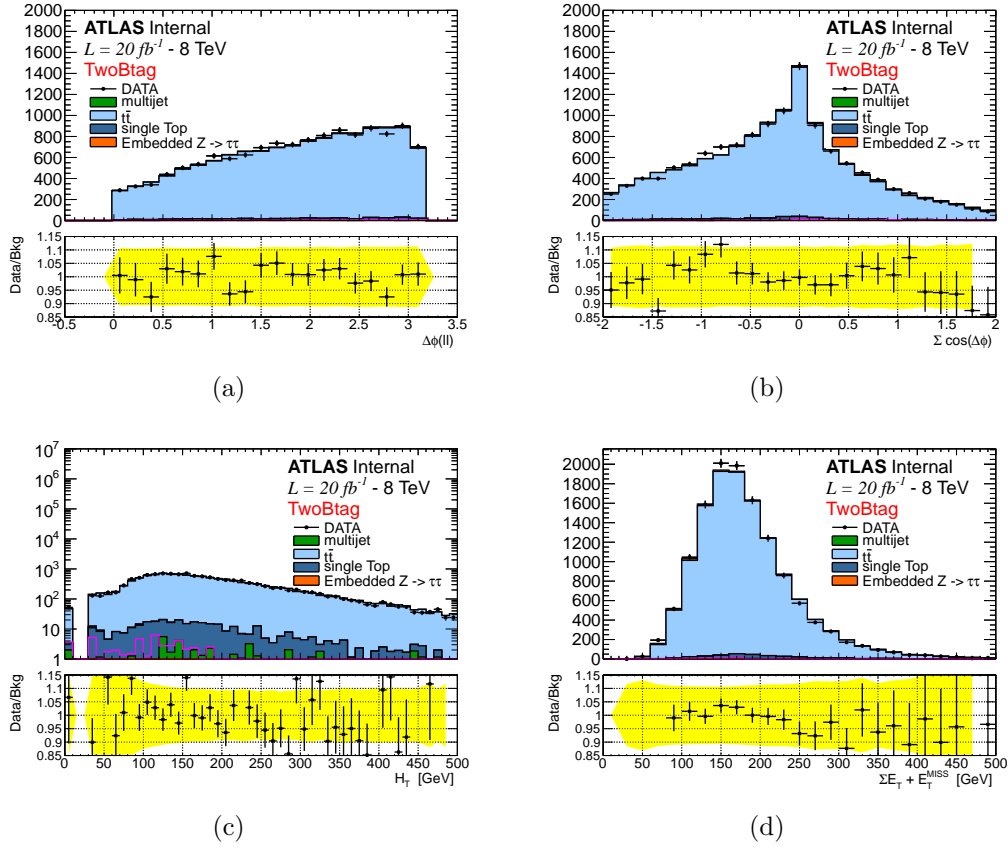


Figure 2.7: Distributions of a)  $\Delta\phi(e - \mu)$ , b)  $\Sigma \cos \Delta\phi$ , c)  $\Sigma L_T + E_T^{miss}$  and d)  $H_T$ , for both data and MC in the  $t\bar{t}$  control region. The uncertainty on the points for the ratio plot show the statistical uncertainty on the data to background ratio, whereas the yellow band show the total systematic uncertainty on this ratio.

### 2.2.3 Multi-jet Background

The QCD multi-jet background represents an important background, especially in the b-veto category, due to its high cross-section and the relatively low cut on lepton  $p_t$  used in this analysis. This background is evaluated by a data-driven technique, the so-called ABCD method. The ABCD method consists of splitting the data sample in four regions: the signal region (SR) and three control regions (CR), where the control regions are mutually orthogonal and designed to be enriched in multi-jets events. The four regions are defined by using the charge correlation between the leptons and isolation selections. With isolation is intended the sum of the energy deposit in a cone of fixed size around the lepton, this variable can be defined using calorimetric energy deposition or track momentum measurement done by the inner detector. To obtain regions rich in multi-jet background, the selections on both the calorimetric and tracking isolation are inverted with respect to the nominal ones defining anti-isolated leptons, is then possible to define four regions: opposite sign (OS) or same sign (SS) with respectively isolated or anti-isolated leptons. Historically the letters A-D are assigned to this regions for a

Region	Lepton Charge	Lepton Isolation
A (signal region)	OS	isolated
B	SS	isolated
C	OS	anti-isolated
D	SS	anti-isolated

Table 2.2: QCD background estimation control regions, defined by having leptons with opposite signs (OS) or same signs (SS) and by having the leptons either isolated or anti-isolated.

quicker reference as defined in Table 2.2.

An assumption of the ABCD method is that multi-jet backgrounds populate the OS and SS events independently of lepton isolation criteria and hence that the ratio of OS/SS events is uncorrelated with the lepton isolation selections. In this case, the number of QCD events in the signal region  $A$  can be estimated from the yield of multijet events in the control regions  $B$ ,  $C$  and  $D$ , using the equation

$$N_A = N_B \times \frac{N_C}{N_D} = N_B \times R_{QCD} \quad (2.1)$$

To obtain the multijet yields in the data CRs, the contamination from electroweak (W+jets, Z+jets and dibosons) and top processes ( $t\bar{t}$  and single top production) are subtracted in each control region using the MC prediction for their event yield. Tables 2.3 and 2.4 show the event yield for each CR throughout the full cut-flows, along with the predictions of non-QCD multi-jets events which are subtracted. Signal contamination has been checked in all the three control regions for different mass points. For the range of  $m_A$  and  $\tan\beta$  considered in this analysis, the highest signal contamination is seen in region B for the mass point  $m_A = 300$  GeV, where at  $\tan\beta = 50$  a contamination of 0.2% is observed. This value is mainly due to b-associated production and, as it scales with the cross section, for  $\tan\beta = 20$  would be an order of magnitude smaller.

Shapes of kinematic distributions for QCD events are taken from the control region B, even though this region suffers from lower statistics than either region C or D. This choice is made to avoid a shape bias due to isolation requirements at trigger level. Figure 2.8 shows the comparison between the electron  $p_t$  distributions in isolated and anti-isolated events, both for SS control regions. Here high  $p_t$  electrons are suppressed due to isolation requirement of the trigger. Eventually the trigger isolation requirement could bias also the ratio OS/SS - this possibility has been checked carefully in a dedicated study and reported in Appendix ???. To a good approximation, such trigger effects cancel out in the ratio OS/SS, so no systematic is applied to the ratio because of this.

To test the ABCD method predictions an additional control region has been defined with the following selections:

- $E_T^{miss} < 20$  GeV
- $H_T < 70$  GeV and  $\sum L_T + E_T^{miss} < 50$  GeV

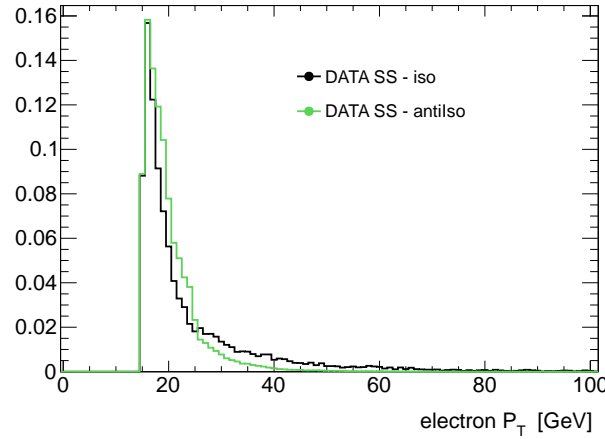


Figure 2.8: Comparison of the electron  $p_t$  distribution in region B and region D, showing the bias due to the trigger. The histograms are normalised to the same area.

- $0 < MMC_{mass} < 80$  GeV

Figure 2.9 shows the  $MMC_{mass}$  distribution for this region with and without b-tagging requirements. Agreement between data and the background model is found in this control region within statistical and detector related systematics uncertainty.

Systematic uncertainties are assigned on the scaling factor  $R_{QCD}$  and on the shape of the discriminating variable  $MMC_{mass}$  to take into account any correlation between isolation and charge of the leptons, details on the systematic uncertainty evaluation are addressed in Section 2.3.

#### 2.2.4 $Z \rightarrow \tau\tau + \text{Jets}$ Background: Embedding Technique

The background from  $Z \rightarrow \tau\tau$  decays is the major background to this analysis, a good understanding of it is then extremely important. Unfortunately, for a light Higgs boson, it is impossible to completely separate  $Z \rightarrow \tau\tau$  decays from the signal and signal free data control region cannot be defined. However, thanks to the small Higgs coupling to muons,  $Z \rightarrow \mu\mu$  decays provide a good starting point to model  $Z \rightarrow \tau\tau$  events in a data-driven way. An hybrid Data-MC sample, known as "Embedding" is used to model the  $Z \rightarrow \tau\tau$  background:  $Z \rightarrow \mu\mu$  candidates are selected in data, then the two muons from the  $Z$  decay are substituted with the decay products from simulated taus, this means that also the energy in a cone around the muon is subtracted and substituted with the one from tau decay, those taus have the same kinematics as the original muons. Further details may be found in [40, 41].

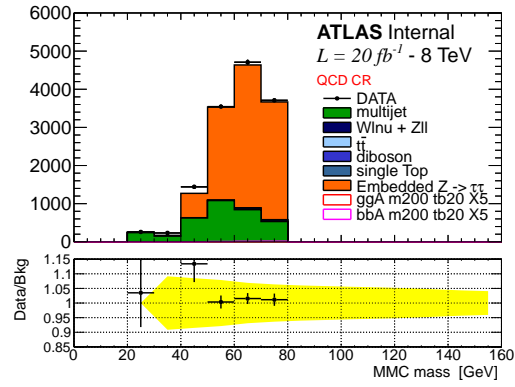
There is no simulation of the trigger in the embedding samples, the event yield is normalised to ALPGEN  $Z \rightarrow \tau\tau$  at preselection stage. Furthermore a set of corrections, as described in [42], are applied to unfold from the trigger and muon reconstruction efficiency of the original  $Z \rightarrow \mu\mu$  events, then trigger and reconstruction efficiency for muon and electron is emulated by the use of event weight.

Selection		B	C	D	$R_{QCD}$
Preselection	Data	6189	604628	312901	$1.929 \pm 0.004$
	non-QCD	$2510 \pm 180$	$1090 \pm 30$	$730 \pm 35$	
B-tag	Data	419	44619	27257	$1.64 \pm 0.01$
	non-QCD	$215 \pm 10$	$310 \pm 12$	$277 \pm 13$	
$\Delta\phi(e - \mu)$	Data	230	38810	23316	$1.67 \pm 0.01$
	non-QCD	$104 \pm 6$	$200 \pm 10$	$175 \pm 7$	
$\sum \cos \Delta\phi$	Data	149	31379	18779	$1.67 \pm 0.02$
	non-QCD	$67 \pm 5$	$127 \pm 8$	$114 \pm 6$	
$\sum H_T$	Data	83	27781	15626	$1.78 \pm 0.02$
	non-QCD	$23 \pm 4$	$25 \pm 3$	$22 \pm 3$	
$\sum L_T + E_T^{miss}$	Data	71	27735	15590	$1.78 \pm 0.02$
	non-QCD	$10 \pm 3$	$22 \pm 3$	$18 \pm 2$	
$MMC_{mass} > 0.$	Data	70	27634	15522	$1.78 \pm 0.02$
	non-QCD	$9 \pm 3$	$20 \pm 3$	$17 \pm 2$	

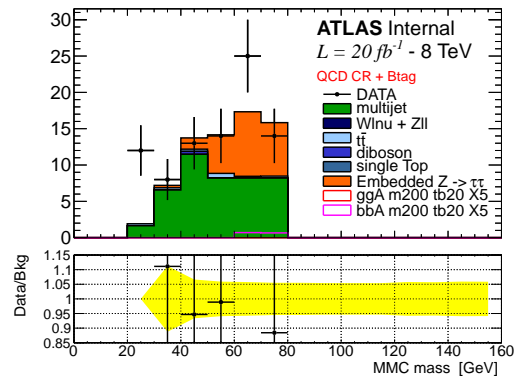
Table 2.3: QCD background estimation as a function of the analysis selections for the b-tagged category. The yields for the different control regions, as well as the scaling factor  $R_{QCD}$ , are reported. The error on the  $R_{QCD}$  is statistical only.

Selection		B	C	D	$R_{QCD}$
Preselection	Data	6189	604628	312901	$1.929 \pm 0.004$
	non-QCD	$2510 \pm 180$	$1090 \pm 30$	$730 \pm 35$	
B-veto	Data	5673	558217	284847	$1.960 \pm 0.004$
	non-QCD	$2220 \pm 180$	$710 \pm 30$	$415 \pm 30$	
$\Delta\phi(e - \mu)i$	Data	4610	532583	271404	$1.962 \pm 0.005$
	non-QCD	$1700 \pm 170$	$580 \pm 30$	$345 \pm 30$	
$\sum \cos \Delta\phi$	Data	3417	486747	247712	$1.965 \pm 0.005$
	non-QCD	$1120 \pm 100$	$370 \pm 20$	$230 \pm 20$	
$MMC_{mass} > 0.$	Data	3177	479967	244276	$1.965 \pm 0.005$
	non-QCD	$1000 \pm 100$	$300 \pm 17$	$190 \pm 20$	

Table 2.4: QCD background estimation as a function of the analysis selections for b-veto category. The yields for the different control regions, as well as the scaling factor  $R_{QCD}$ , are reported. The error on the  $R_{QCD}$  is statistical only.



(a)



(b)

Figure 2.9:  $MMC_{mass}$  distribution for QCD cross check regions defined in section 2.2.3 (a) and for the same CR when in addition one b-tagged jet is required (b).

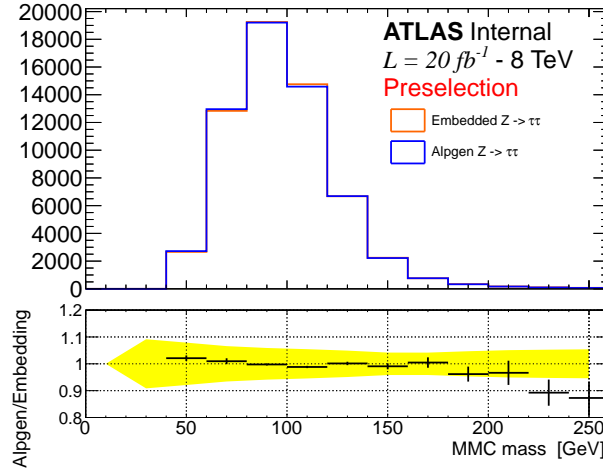


Figure 2.10: Comparison between the embedded  $Z \rightarrow \tau\tau$  and ALPGEN for  $MMC_{mass}$  distributions.

The Embedding technique has been validated in several studies, detailed in [40, 42], which show a good description of data and  $Z \rightarrow \tau\tau$  MC by Embedding. In the context of this analysis, figures 2.10 and 2.11 show comparisons of various kinematic variables between data, embedding and ALPGEN  $Z \rightarrow \tau\tau$  events at preselection. No significant deviation is seen between the  $MMC_{mass}$  distribution of the embedding and ALPGEN samples. However other relevant variables for this analysis, such as the  $E_T^{miss}$  and the number of b-jets, are slightly better described by embedding. Additional plots are reported in appendix ??.

The Embedding sample is based on selecting  $Z \rightarrow \mu\mu$  candidates in data, the selections assure a rather pure  $Z \rightarrow \mu\mu$  sample, however further selections used in this analysis, for example the b-tagging requirements, could enhance the contamination fraction from other processes in the embedding sample. Hence dedicated studies have been made to estimate the  $t\bar{t}$  and QCD multi-jet contamination in the embedding sample. The  $t\bar{t}$  contamination is estimated by evaluating the embedding sample yield in a two b-tag control region, as described in Section 2.2.2. These events are assumed to be solely from  $t\bar{t}$  and their yield in the signal region is extrapolated using POWHEG-PYTHIA  $t\bar{t}$  simulation sample. Table 2.5 shows a summary for the top contamination in embedding and this contamination is hence taken to be negligible. The multi-jet contamination can be estimated starting from the embedding yield of opposite sign anti-isolated events (region C). Assuming all events in this CR as QCD multi-jet events, the contamination in the SR can be estimated using the ABCD method (see Section 2.2.3). The  $R_{QCD}$  factor used in this case is evaluated using a mu-mu final state CR with the same kinematics selections used in the definition of the embedding sample. Table 2.6 shows the estimated contamination of QCD multi-jet in embedding. We consider contamination effects negligible.



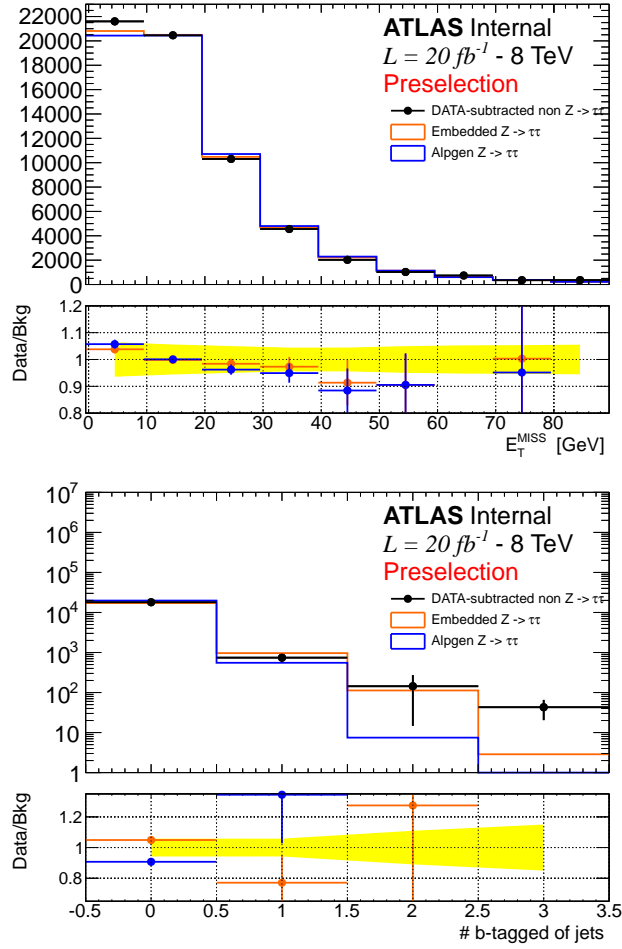


Figure 2.11: Comparison between embedded  $Z \rightarrow \tau\tau$  and ALPGEN for  $E_T^{miss}$  and the number of b-tagged jets distributions. Data are superimposed, with the contribution of non- $Z \rightarrow \tau\tau$  are subtracted.

	Embedding yield in CR	Transfer factor	Estimated events in SR	Contamination
b-tag	$84 \pm 9$	$(2.6 \pm 0.1) \times 10^{-2}$	$2.2 \pm 0.2$	0.5 %
b-veto	$84 \pm 9$	$(1.74 \pm 0.02) \times 10^{-1}$	$15 \pm 2$	0.03 %

Table 2.5: Evaluating embedding  $t\bar{t}$  contamination using a two b-tag CR. The transfer factor is the multiplicative factor that allows to estimate events in SR from the CR.

	Embedding yield in CR	Transfer factor	Estimated events in SR	Contamination
B-tag	$12 \pm 3$	$(7 \pm 1) \times 10^{-3}$	$(8.4 \pm 0.3) \times 10^{-2}$	0.03 %
B-veto	$390 \pm 20$	$(2.5 \pm 0.1) \times 10^{-2}$	$10.0 \pm 0.5$	0.02 %

Table 2.6: Evaluating embedding contamination due to QCD multi-jet using ABCD method, the CR here is with OS anti-isolated events (region C). The transfer factor is the multiplicative factor that allows to estimate events in SR from the CR, in this case is  $N_B/N_D$  and is evaluated using mu-mu final state with the same kinematic selection used in the definition of the embedding sample.

## 2.3 Systematic Uncertainties

This section describes the range of systematic uncertainties that are relevant for this analysis. To account for differences in the detector responses between simulation and data a set of corrections are applied either at object reconstruction level and at event level. The uncertainties on such corrections are considered as detector-related systematic uncertainties and are detailed in section 2.3.1. Further systematic uncertainties related to data-driven methods for backgrounds estimation are described in section ???. For samples which rely on MC simulation, theory-related systematics, which include uncertainties on the cross-section and uncertainties on the acceptance of analysis selections, are finally described in section 2.3.4.

Each single systematic can contribute separately to the uncertainty on the final event yield and on the shape of the  $MMC_{mass}$  distribution that is used as the discriminating variable for the limit derivation. These shape systematics are documented in appendix ???. Systematic uncertainties that do not effect the mass shape distribution and have an impact on the event yield of a samples of less than 0.5% are neglected in the final limit calculations.

### 2.3.1 Detector-related Systematics Uncertainties

Here systematic uncertainty related to object reconstruction and event corrections are addressed, those corrections are based on the measure of some relevant parameter, each of those parameters correspond to a "nuisance parameter" in our probability model as described in Section ???. Each parameter is varied independently (one sigma up or down) according with its uncertainty and the impact on the analysis yield for each sample is evaluated. In the following, detector related uncertainty are described with some more details, table 2.7 and 2.8 briefly summarize the impact on the samples yield for the most significant systematic uncertainty considered.

**Luminosity** The integrated luminosity of the 8 TeV data recorded at ATLAS during 2012 is measured to be  $20.3 \text{ fb}^{-1}$  [66], its uncertainty is 2.8%.

**Pileup** Simulated events are re-weighted to reproduce the average interactions per bunch crossing,  $\langle \mu \rangle$ , seen in data. Those event weights has an uncertainty

wich is propagated to each simulated sample.

**Trigger Efficiency** Trigger efficiency is corrected in simulation to match (as a mean value) the one in data, those correction weights are evaluated as a function of  $p_t$  and  $\eta$  of the leptons and have associated uncertainties. Systematic uncertainties on both the single electron and electron-muon trigger efficiency are considered independently, those uncertainty range approximately 1-2%.

In the embedding sample, the trigger is emulated by applying weights to the event topology in order to recover the right trigger efficiency, those weights are related to the one just described and have similar uncertainty. Trigger efficiency uncertainty for Embedding are considered uncorrelated with the one of other samples.

**Electrons** Two types of uncertainty on reconstructed electron objects are considered: the first are related to electron identification and reconstruction efficiencies ("Electron ID"), the second type are related to electron energy scale and resolution corrections. The energy scale uncertainties are split into a set of six different nuisance parameters, however only few of them give a non negligible contribution, in particular two of them are found to affect the shape of the  $MMC_{mass}$  distribution and are considered independently, those are the uncertainty that arise from the  $Z \rightarrow ee$  momentum measurement ("Electron Zee") and the one related to low momentum electrons ("Electron LOWPT"). We sum in quadrature all the other uncertainties related to energy scale and resolution ("Electron E.").

**Muons** The uncertainty on muon identification efficiency depends on the charge and momentum of the muon. Typically these uncertainties are of the order of a fraction of percent, and are referred as "Muon ID". The uncertainties on the muon energy scale and resolution are considered independently for the inner detector and muon spectrometer measurements, then are added in quadrature to estimate the final effect ("Muon E").

**Taus** Hadronic tau object are only used in the analysis as a veto. Uncertainties on both tau energy scale and identification efficiency have been investigated and are found to be negligible for this analysis.

**Jets** The systematic uncertainties on the Jet Energy Scale (JES) are split up into multiple sets of nuisance parameters, which are related to different effects and components, for example: the sensitivity to pileup or to the flavour composition of the jet. The overall uncertainty on the JES ranges between 3% and 7%, depending on the  $p_t$  and  $\eta$  of the jet. To give an idea of the effect that these uncertainty have on the analysis yield their sum in quadrature is reported in table ?? ("JES"), this is just a simplification used here as illustration and in the limits extraction they are considered separately. Systematic uncertainty due to jet resolution ("Jet Resolution") are obtained by smearing the jet energy according to its uncertainty.

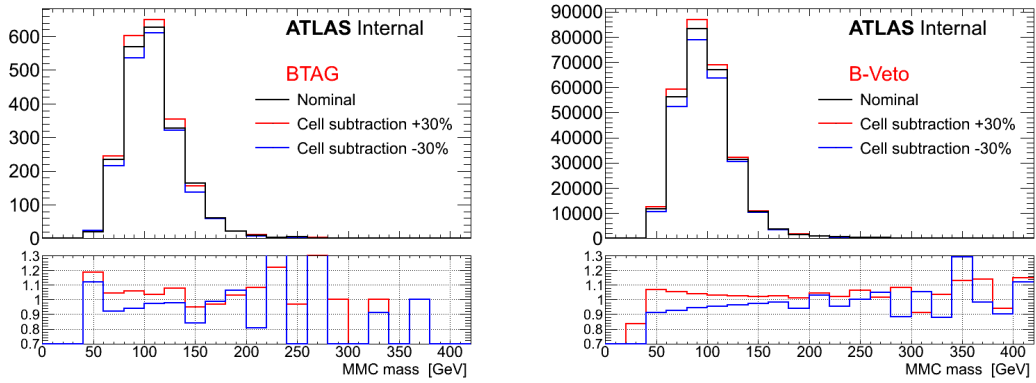


Figure 2.12: Embedding MFS systematic uncertainty impact on  $MMC_{mass}$ .

**b-Tagging** is described in chapter ???. Corrections are applied to simulation to match b-tagging efficiency with the one in data, uncertainties on the knowledge of the b-tagging efficiencies for the 70% working point of the MV1 b-tagger are considered in this analysis. Uncertainties for b-quark, c-quark and light or gluon initiated jets, are considered separately and referred respectively to as "B Eff.", "C Eff." and "L Eff.". The tagging and mistagging efficiencies are considered to be totally anti-correlated.

**Missing Transverse Energy** The effect of the energy scale uncertainties for all the physics objects is propagated to the  $E_T^{miss}$  calculation. In addition uncertainty on the energy scale and resolution due to the remaining calorimeter energy deposit, the so called "soft-terms", are considered. All the uncertainty on  $E_T^{miss}$  are independently propagated through the analysis and are added in quadrature, this final term is referred as "MET" uncertainty.

### 2.3.2 $Z \rightarrow \tau\tau$ Embedding Systematics

An important element of the embedding method is the subtraction of the calorimeter cells associated with the muons in the original  $Z \rightarrow \mu\mu$  event and their substitution with those from the simulated tau decays. To make a conservative estimate of the systematic uncertainty on this procedure, the energy of the subtracted cells is scaled up or down by 30%. The analysis is repeated with those modified samples and the relative uncertainty is referred as EMB\_MFS. The effect of this uncertainty affects mainly the shape of the  $MMC_{mass}$  distribution, shown in figure ??.

In the selection of the  $Z \rightarrow \mu\mu$  sample only a loose requirement on muon track isolation is required. A different selection on the muon isolation may effect the selected sample by modifying the topology of the event, changing the non- $Z \rightarrow \mu\mu$  contamination or the activity in the calorimeter. To estimate the importance of these effects in our embedding sample, the isolation selection on the muons in the original  $Z \rightarrow \mu\mu$  events is tightened, a looser selection would have limited impact because of isolation requirements at trigger level. The resulting uncertainty, referred

Source	b-tag category uncertainties (%)				
	Signal bbH	Signal ggH	$Z \rightarrow \tau\tau$	Top	Other
Electron SF	2.3	2.0	2.8	1.8	2.0
Electron E.	0.7	1.2	0.5	0.5	0.9
Electron LOWPT	0.4	0.0	0.4	0.1	0.4
Electron Zee	0.3	0.6	0.4	0.6	0.5
Muon ID	0.3	0.3	0.3	0.3	0.3
Muon E.	0.5	7.7	0.1	0.1	0.2
Trigger Single Ele.	0.7	0.5	0.5	0.8	0.8
Trigger Dilepton	1.0	1.2	1.4	0.6	0.6
Embedding MFS	-	-	0.0	-	-
Embedding Iso.	-	-	1.3	-	-
JES Effective-1	0.5	0.0	-	3.8	2.3
JES Effective-2	0.6	7.8	-	5.5	2.5
JES Effective-3	0.5	0.0	-	2.2	2.0
JES EtaModelling	1.1	0.0	-	4.0	2.1
JES Pileup-NPV	0.5	0.0	-	1.2	0.3
JES Pileup-Rho	0.8	7.8	-	2.8	2.2
JES FlavComp.	1.2	6.3	-	2.1	4.5
JES FlavResp.	1.3	0.0	-	1.4	1.9
JES BJet	1.2	0.0	-	4.2	1.2
JER	1.4	6.3	-	2.9	3.0
B Eff	10.2	5.3	-	2.6	5.0
C Eff	0.2	2.8	-	0.0	1.2
L Eff	0.4	8.0	-	0.1	1.2
Pileup	0.4	0.7	0.4	0.4	0.9
MET	0.7	11.0	0.2	1.0	1.2
Acceptance					
Cross Section	-	-	5.0	5.5	7.1
Luminosity	2.8	2.8	2.8	2.8	2.8

Table 2.7: Summary of the effect of the experimental and theoretical systematic uncertainties on the yields of the different fusion with  $m_A = 120$  GeV and  $\tan\beta = 20$ . Systematic uncertainties with a negligible effect are listed with a value of 0.0 and those that lead to a shape uncertainty are noted with the symbol (s). Note that the same naming convention is respected for the actual nuisance parameters in the limit framework.

Source	b-veto category uncertainties (%)				
	Signal bbH	Signal ggH	$Z \rightarrow \tau\tau$	Top	Other
Electron SF	2.4	2.3	2.9 (s)	1.4	1.6
Electron E.	0.4	0.5	0.4	0.5	0.9
Electron LOWPT	0.3	0.5	0.4 (s)	0.0	1.2
Electron Zee	0.4	0.4	0.4 (s)	0.1	0.3
Muon ID	0.3	0.3	0.3	0.3	0.3
Muon E.	0.1	0.1	0.1	0.5	0.5
Trigger Single Lep.	0.6	0.6	0.5	0.9	0.9
Trigger Dilep.	1.0	1.0	1.3	0.2	0.3
Embedding MFS	-	-	0.1 (s)	-	-
Embedding Iso.	-	-	0.0 (s)	-	-
JES Effective-1	0.2	0.2	-	0.4	0.4
JES Effective-2	0.2	0.3	-	0.3	0.5
JES Effective-3	0.2	0.2	-	0.2	0.3
JES EtaModelling	0.1	0.1	-	0.1	0.3
JES Pileup-NPV	0.3	0.1	-	0.1	0.3
JES Pileup-Rho	0.3	0.2	-	0.5	0.5
JES FlavComp.	0.1	0.2	-	0.2	0.5
JES FlavResp.	0.2	0.4	-	0.3	0.6
JES BJet	0.2	0.0	-	0.5	0.1
JER	0.5	0.3	-	0.6	0.3
B Eff	1.8	0.0	-	12.0	0.8
C Eff	0.0	0.1	-	0.1	0.0
L Eff	0.0	0.1	-	0.2	0.1
Pileup	0.5	0.8	0.4	0.3	0.3
MET	0.2	0.8	0.1	0.2	0.5
Acceptance					
Cross Section	-	-	5.0	5.5	5.9
Luminosity	2.8	2.8	2.8	2.8	2.8

Table 2.8: Summary of the effect of the experimental and theoretical systematic uncertainties on the yields of the different samples used in the b-veto channel. Here "Other" refers to the sum of all the remaining samples:  $W \rightarrow l\nu$ , diboson,  $Z \rightarrow ll$  and single top. The signal samples listed here are b-associated production and gluon fusion with  $m_A = 120$  GeV and  $\tan\beta = 20$ . Systematic uncertainties with a negligible effect are listed with a value of 0.0 and those that lead to a shape uncertainty are noted with the symbol (s). Note that the same naming convention is respected for the actual nuisance parameters in the limit framework.

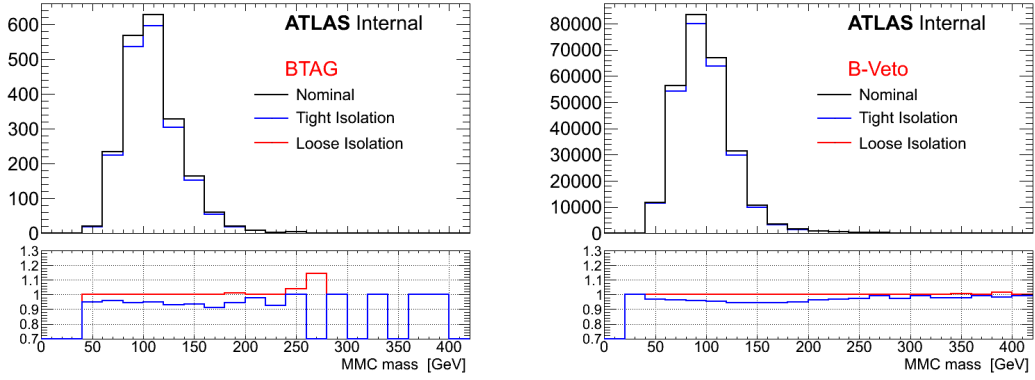


Figure 2.13: Embedding Isolation systematic uncertainty impact  $MMC_{mass}$ .

to as EMB ISO, affects both the yield and the  $MMC_{mass}$  shape of the embedding samples, as shown in figure ??.

Finally, because the normalisation of the embedding sample is determined by the use of the ALPGEN sample, the relative cross section and luminosity uncertainties are assigned. In addition all the detector-related systematic uncertainties relevant to the decay products of the simulated tau decay are propagated to the embedding sample.

### 2.3.3 QCD Multi-Jet Systematics

In this analysis the QCD multi-jet background is estimated via the ABCD method, as described in Section 2.2.3. This technique relies strongly on the assumption that the lepton isolation variables are independent from the charge correlation between the two leptons. Systematic uncertainties are assigned to take into account deviations from this assumption. First we consider the correlation between  $R_{QCD}$  and the lepton isolation selections, then we compare the result with an auxiliary method.

Figure 2.14 shows the  $R_{QCD}$  factor, the ratio between the QCD yields in region C and D, as a function of the lepton isolation selections (red points). As described previously, the expectation from non-QCD backgrounds is subtracted from the data in regions C and D. To estimate the uncertainty on the value of  $R_{QCD}$  an additional transfer factor is defined as follows:  $R_{QCD}^{iso} = \hat{A}/\hat{B}$ , where  $\hat{A}$  and  $\hat{B}$  are semi-isolated OS and SS regions defined with the lepton isolation larger than the standard requirement, but less than a sliding cut. Once more, the non-QCD contributions are subtracted from the data yields. The regions  $\hat{A}$  and  $\hat{B}$  are chosen to be semi-isolated due to the high contamination of non-QCD background and possible signal in region A and B. Figure 2.14 shows  $R_{QCD}^{iso}$  as a function of the lepton isolation selections (black points). The difference between  $R_{QCD}$  and  $R_{QCD}^{iso}$  in the vicinity of the standard cut value is then assigned as a systematic uncertainty on  $R_{QCD}$ . Using the point where the cuts on the lepton isolation are twice their standard values, a systematic uncertainty of 15% is found. The plot in Figure 2.14 is made at preselection level, similar plots using the full selection for the two categories are in Appendix ??.

Selection	$R_{QCD}$	$R_{QCD}^{AB}$	$R_{QCD}^{iso}$
Preselection	$1.929 \pm 0.004$	$2.12 \pm 0.17$	$2.22 \pm 0.16$
B-veto	$1.965 \pm 0.005$	$2.10 \pm 0.16$	$2.22 \pm 0.16$
B-tag	$1.78 \pm 0.02$	$1.9 \pm 0.9$	$2.0 \pm 0.8$

Table 2.9: Comparison between  $R_{QCD}$ ,  $R_{QCD}^{AB}$  and  $R_{QCD}^{iso}$  for early stage in the cutflow, only b-tag and b-veto requirement are applied after preselections. Reported is statistical uncertainty only.

An additional method, used as a crosscheck, considers calculating  $R_{QCD}$  as the ratio between the estimated QCD contributions in region A and B. Here the non-QCD contributions are once more subtracted from data. However the large contribution of this non-QCD background, along with lack of statistics and possible signal contamination, lead to this only being used as a cross check. Table 2.9 shows a comparison between  $R_{QCD}$  and  $R_{QCD}^{AB}$  for the two categories at the preselection stage of the cutflow, where signal contamination is negligible. Agreement is seen between  $R_{QCD}$  values in the two regions, within statistical uncertainties.

The actual implementation in the limit framework of the ABCD method follows that suggested in [62]. Here three free parameters are fitted: number of multi-jet events in region B,  $N_B^{QCD}$ , factor that extrapolates from SS region to OS regions,  $R_{QCD}$ , and the factor that extrapolates from isolated to anti-isolated regions  $R_{BD}$ . Neglecting signal contributions, the following equations can be written for the event yield of the B,C and D control regions:

$$N_B = N_B^{BKG} + N_B^{QCD}$$

$$N_C = N_C^{BKG} + N_B^{QCD} \times R_{QCD} \times R_{BD}$$

$$N_D = N_D^{BKG} + N_B^{QCD} \times R_{BD}$$

where  $N^{BKG}$  represent the prediction of non-QCD background in the relative regions. The estimate of multi-jet event yield in SR will be then  $N_B^{QCD} \times R_{QCD}$ . This method is particularly powerful because in the best fit of  $R_{QCD}$  the statistical and systematics uncertainty for non-QCD backgrounds and data will be considered.

The difference in  $MMC_{mass}$  shape observed between the OS and SS anti-isolated regions (C and D) is shown in Figure 2.15. This effect is within the uncertainty on  $R_{QCD}$  of the ABCD method, hence no correction factor is applied to the mass shape. We assume, however, that there could be the same shape difference in the isolated regions. Hence a shape uncertainty is assigned in the limit machinery to region B with this deviation. Further shape uncertainties due to non-QCD background subtraction are found to be negligible. The uncertainty due to the use of an isolation requirement at trigger level is discussed in Appendix ?? and is found to be negligible.



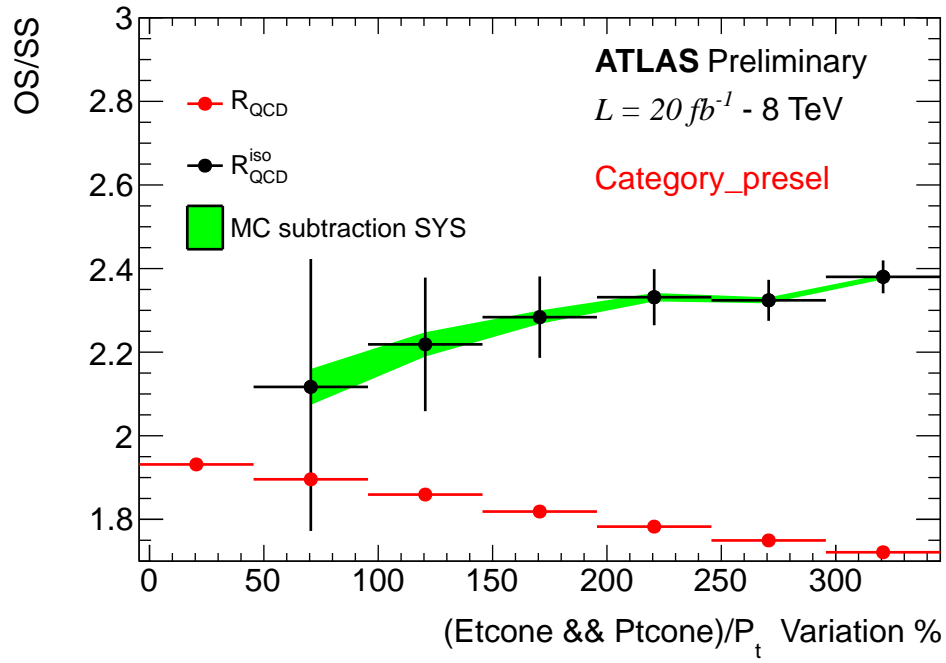


Figure 2.14: OS/SS ratio as a function of lepton isolation variable selections. The selections are varied as a percentage relative to the standard lepton isolation cut values (0 in the plot). The red points show the anti-isolated scale factor  $R_{\text{QCD}}$ , i.e. the ratio between regions C and D. The black points show the isolated SF, which is defined as the ratio between region  $\hat{A}$  and  $\hat{B}$ , where the leptons have isolation values larger than the nominal value but smaller than the sliding cut on X axis.

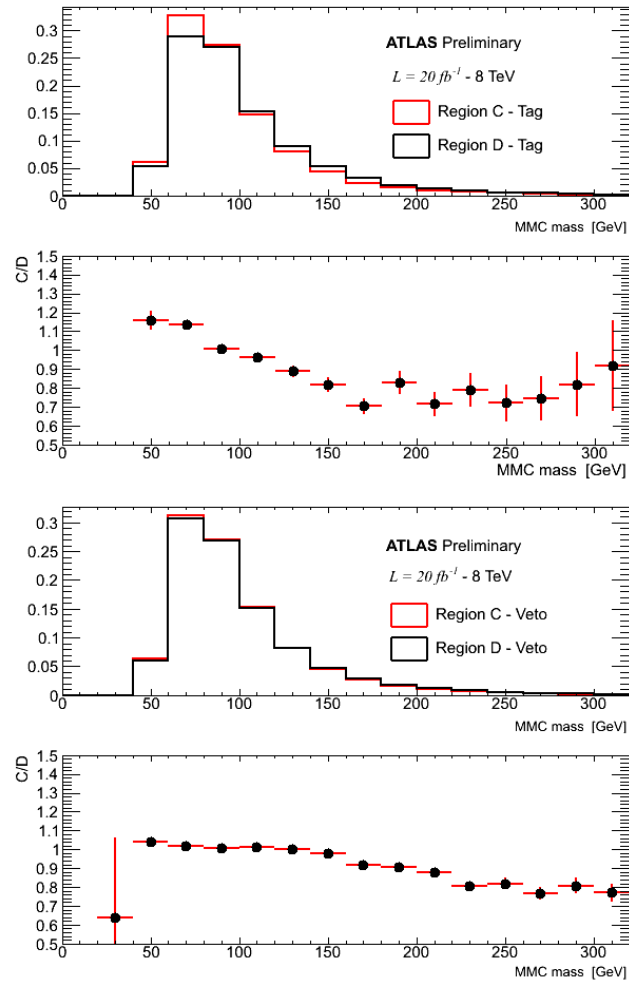


Figure 2.15: Shape differences for the b-tag and b-veto categories between the ABCD regions C and D.

Generator	Process	Uncertainty
ALPGEN	$Z \rightarrow \tau\tau/ee/\mu\mu$	$\pm 5\%$
POWHEG	$t\bar{t}$	$\pm 5.5\%$
ALPGEN	$W \rightarrow \tau\nu/e\nu/\mu\nu$	$\pm 5\%$
AcerMC	single top	$\pm 13\%$
HERWIG	dibosons	$\pm 6\%$
SHERPA	$bbA/h/H$ ( $m_A \geq 120$ GeV)	$-( < 20)\%, +( < 9) \%$
SHERPA	$bbA/h/H$ ( $m_A = 110$ GeV)	$-( < 25)\%, +( < 9) \%$
SHERPA	$bbA/h/H$ ( $m_A = 100$ GeV)	$-( < 28)\%, +( < 9) \%$
SHERPA	$bbA/h/H$ ( $m_A = 90$ GeV)	$-( < 30)\%, +( < 9) \%$
POWHEG	$ggA/h/H$ ( $m_A \leq 300$ GeV)	$< 15\%$

Table 2.10: Cross-section uncertainties for background and signal samples. The reported signal samples are all for  $\tan\beta = 20$ .

### 2.3.4 Theoretical Uncertainties

Uncertainties on the cross-sections that have been used to normalise simulation samples to data are reported in Table 2.10. These uncertainties include contributions due to parton distribution functions (PDFs), the choice of the value of strong coupling constant, and the renormalisation and factorisation scales. Furthermore the uncertainties on signal cross-section depends on  $\tan\beta$ , the Higgs boson type ( $A/h/H$ ) and mass.

The effect of systematic uncertainties due to various MC tuning parameters, underlying event and lepton kinematic description is considered. Since the effect on the invariant mass distribution of the di-tau system from these systematic uncertainties is negligible (as an example see Figure 2.16), only the variation in acceptance is considered as systematic uncertainty. The acceptance uncertainties for the ALPGEN Z MC, used for the normalisation of the embedded sample, are estimated at lepton preselection to be 4% [64]. Since additional selections are applied directly to the embedded sample, no further acceptance uncertainties is considered. Acceptance systematics on  $t\bar{t}$  simulated events are still to be determined. The acceptance uncertainties on diboson and single top production are assumed to be 2%. Uncertainties on signal acceptance have been estimated by producing samples with varied MC generator parameters and evaluating, at truth-level, the effect of analysis selections on leptons, taus and jets. This truth-level study is implemented within the Rivet framework [68], where additionally b-tagging is performed by identifying b-quarks and applying a weighting according to the estimated ATLAS b-tagging efficiencies [65]. The variation of the acceptance with respect to the nominal MC tune has been considered as a source of systematic uncertainty. For signal a total acceptance uncertainty varies from 4% to 30% depending on  $m_A$ , production process and on the analysis category.

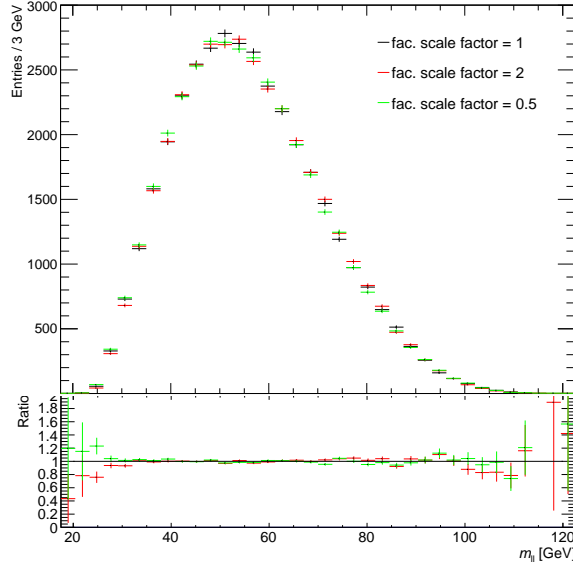


Figure 2.16: Comparison of the visible mass of tau decay products after factorisation scale variation for the b-veto category on a gluon fusion signal sample.

## 2.4 Results

### 2.4.1 LHC Procedure For Limits Setting

A detailed description of the LHC procedure for Higgs search can be found in [?, ?], in the following a brief summary is given. Statistical tests are used for quantify an observation or to set an exclusion limit, in search for new phenomena hypothesis testing is performed by means of two hypothesis: the *background only*  $H_0$  and the *signal+background*  $H_1$ . As its has allready been outlined in section ??, any statistical test is based on probability distribution, in particular is important to define what is called a "likelihood": taking the marked Poisson probability density function (p.d.f.) (??) calculating it for a set of data one obtaine what is called likelihood function:

$$\mathcal{L}(\text{data}|\mu, \boldsymbol{\theta}) = \text{Poisson}(\text{data}|\mu \cdot s(\boldsymbol{\theta}) + b(\boldsymbol{\theta})) \cdot f(\boldsymbol{\theta}|\hat{\boldsymbol{\theta}}) \quad (2.2)$$

of the data under a certain hypothesis, which now will be only function of the parameter  $\mu$  and of the nuisance parameter  $\boldsymbol{\theta}$ , note that is not anymore a p.d.f. and not normalized to one. However its value will be decreasing if the hypothesis under test is unlikely to happen with the given dataset, one can define what's the best value of a parameter that describes the data via maximising the likelihood, obtaining a so called maximum likelihood estimator. The Poisson distribution in equation (2.2) stands for a product of Poisson probabilities to observe events in the bin  $i$  of an histogram:

$$\prod_i \frac{(\mu s_i + b_i)^{n_i}}{n_i!} e^{-\mu s_i - b_i}$$

while the  $f(\boldsymbol{\theta}|\hat{\boldsymbol{\theta}})$  is the p.d.f. for a given set of nuisance parameter  $\boldsymbol{\theta}$  with their best estimate  $\hat{\boldsymbol{\theta}}$ .

To compute the compatibility of the data with the  $H_0$  and  $H_1$  hypothesis, and then exclusion limits one needs to define a test statistic. The test statistic, which has already been met in section ??, is a function of the data which returns a real value. One can in principle use any test statistic, however, given the size of the test (probability to reject the null hypothesis when is true) one would like to have a test statistic which has the highest power  $1 - \beta$  possible (probability to reject the null hypothesis when it is false), this means that the test statistic should have different distribution for the two hypothesis under test. Figure ?? shows an example of the distribution of an hypothetical test statistic for two hypothesis. It has been shown by Neuman-P [?] that in case of simple hypothesis (probability model without any parameter), then the test statistic with the highest power is the ratio of the likelihood calculated with the two hypothesis: The standard procedure at the LHC is to use the following test statistic [?] based on the likelihood ratio:

$$\tilde{q}_\mu = -2 \ln \frac{\mathcal{L}(\text{data}|\mu, \hat{\boldsymbol{\theta}}_\mu)}{\mathcal{L}(\text{data}|\hat{\mu}, \hat{\boldsymbol{\theta}})} \quad \text{with the constraint} \quad 0 \leq \hat{\mu} \leq \mu$$

where  $\hat{\mu}$  and  $\hat{\boldsymbol{\theta}}$  are the maximum likelihood estimators for  $\mu$  and  $\boldsymbol{\theta}$  given the data, whereas  $\hat{\boldsymbol{\theta}}_\mu$  is the maximum likelihood estimator of  $\boldsymbol{\theta}$  given the data but considering a signal strength of value  $\mu$ . to be noted that  $\tilde{q}_\mu$  is increasing with increasing disagreement between data and the  $\mu$  hypothesis under test. The procedure for limits setting follows five steps:

1. The signal hypothesis with signal strength  $\mu$  is assumed, under this assumption a set of *pseudo-data* is generated for different values of  $\mu$ .
2.  $\tilde{q}_\mu$  is calculated for each of the *pseudo-dataset* and each signal hypothesis generating the expected probability density function for  $\tilde{q}_\mu$  given  $\mu$ ,  $f(\tilde{q}_\mu | \mu, \hat{\boldsymbol{\theta}}_\mu, H_1)$ .
3. One does the same thing for the null hypothesis, generate pseudo-data with the distribution of background only and generate the  $f(\tilde{q}_\mu | \mu = 0, \hat{\boldsymbol{\theta}}_0, H_0)$ .
4. Once one has the pdf for the signal and signal + background hypothesis one can define for a given dataset (that can be this time real data or again pseudodata) two p-values for a given value of  $\mu$ , which are the probability to obtain data less compatible with the hypothesis in consideration:

$$p_{s+b} = P(\tilde{q}_\mu > \tilde{q}_\mu^{\text{observed}} | H_1)$$

$$p_b = P(\tilde{q}_\mu > \tilde{q}_\mu^{\text{observed}} | H_0)$$

Calculate the ratio of this two probability and get what is called the  $CL_s = p_{s+b}/p_b$  [?].

5. If for a given  $\mu$  is obtained  $CL_s \leq \alpha$  one states that the signal hypothesis (with that  $\mu$ ) is excluded with  $(1 - \alpha)$   $CL_s$  confidence level. To get the 95% confidence level upper limit on  $\mu$ , denoted as  $\mu^{95}$  one adjust  $\mu$  until  $CL_s = 0.05$ .

This is a quite complicated prescription, however its interpretation is not so different from the usual Neyman Costruction [] of confidence intervals: for each  $\mu$  is possible to define  $\tilde{q}_\mu^{95}$  for which the probability  $P(\tilde{q}_\mu \geq \tilde{q}_\mu^{95} \mid \mu, H_1) = 5\%$ , this means that if  $H_1$  is true one expects  $\tilde{q}_\mu \geq \tilde{q}_\mu^{95}$  in 5% of the cases. With this definition  $\mu^{95}$  would be the value of  $\mu$  that for the observed data gives  $\tilde{q}_\mu = \tilde{q}_\mu^{95}$ , or in other words a p-value of 5%. By costruction, rejecting  $\mu > \mu^{95}$  the hypotesis  $H_1$  will be rejected when is true at most 5% of the time, given the fact that  $\tilde{q}_\mu$  is increasing with increasing discrepancy of the hypotesis with data. The difference with the  $CL_s$  prescription is that here the ratio of p-values is used to define  $\mu^{95}$ , it has been shown that this choice protect the upper limit from down fluctuation of the data, giving a conservative estimate in any case.

## 2.4.2 Exclusion Limits

The procedure described in section 2.4.1 is the one used for the SM Higgs, for the MSSM further complication arise: one has to consider in the signal model three Higgses for which in a particular scenario the masses and cross section are defined for a given point in the  $\tan\beta - m_A$  plane, so the procedure described previously has to be repeated for each point in that plane. For the  $m_h^{max}$  scenario exclusion limits are derived by calculating 95% CLs limits on the cross section of  $bb/gg \rightarrow A/H/h \rightarrow \tau_{lep}\tau_{lep}$  for 15  $\tan\beta$  values (between<sup>2</sup>  $\tan\beta = 5$  and  $\tan\beta = 60$ ), a point in the  $\tan\beta - m_A$  plane is excluded if  $\mu^{95} \leq 1$  for that point, since only a limited number of points in that plane is generated, a linear interpolation is used to determine the  $\tan\beta$  excluded for a given  $m_A$ . The procedure is followed for a set of different CP-odd Higgs masses  $m_A$ : 90, 100, 110, 120, 125, 130, 140, 150, 170, 200, 250 and 300 GeV. The event yield has been compared between data and background expectation in bins of the  $MMC_{mass}$  distribution. The bin sizes were chosen such that there are enough events left for the asymptotic approximation [69] to hold. Table 2.11 compares yields between data and our background model for the two categories at the final stage of the cut flow. Additionally, figure 2.17 shows the  $MMC_{mass}$  distributions for the full b-tag and b-veto categories.

(a)(b)

Figure 2.17: Distributions of the  $MMC_{mass}$  mass for (a) the full b-tag category selection and (b) the full b-veto selection. In these plots the data distributions are not shown.

The resulting exclusion limit on the MSSM parameter space ( $m_A$  vs  $\tan\beta$  plane) are interpreted within the  $m_h^{max}$  benchmark scenario [34] and shown in Figure 2.18. The expected and observed 95% confidence-level limits are shown as solid and dashed black lines, the green and yellow bands correspond to the  $1\sigma$  and  $2\sigma$  error bands. The analysis is sensitive to MSSM Higgs production of  $\tan\beta \geq 13$  for the range  $90 < m_A < 200$  GeV. The observed limit is presently unknown.

<sup>2</sup>The set of  $\tan\beta$  values used is 5, 8, 10, 13, 16, 20, 23, 26, 30, 35, 40, 45, 50, 55, 60

Sample	b-tag category			b-veto category		
	N(event)	Stat.	Syst.	N(event)	Stat.	Syst.
$Z \rightarrow \tau\tau$	418	$\pm 6$		54680	$\pm 60$	
$t\bar{t}$	330	$\pm 10$		2228	$\pm 25$	
Multijet	100	$\pm 15$		3940	$\pm 330$	
$W \rightarrow l\nu$	10	$\pm 6$		650	$\pm 100$	
Diboson	13.1	$\pm 1.8$		2921	$\pm 27$	
Single Top	90	$\pm 6$		443	$\pm 15$	
$Z \rightarrow ll$	0.9	$\pm 0.8$		430	$\pm 40$	
Total	962	$\pm 16$		65290	$\pm 180$	
Signal						
Data	-	-	-	-	-	-

Table 2.11: Comparison between yield in data and the one expected from our background model, b-tag and b-veto category are reported separately.

Figure 2.18: Expected exclusion limits for MSSM Higgs boson production in the MSSM  $m_A$  vs  $\tan\beta$  parameter space.

The outcome of the search is also interpreted in the generic case of a scalar boson produced in the  $pp \rightarrow gg \rightarrow \phi$  or  $pp \rightarrow b\bar{b}\phi$  mode and decaying to a di-tau pair. These limits will be shown in Figure 2.19 for the b-associated and the gluon-gluon fusion production mechanisms separately. All signal systematic uncertainties are implemented in the likelihood for this limit derivation, including the acceptance systematics, with the exception of the signal cross section uncertainties. More information about the limits and their validation can be found in Appendix ??.

### 2.4.3 Summary

A search for neutral MSSM Higgs bosons with the ATLAS detector at the LHC is presented. This analysis is based on an integrated luminosity of  $20.3 \text{ fb}^{-1}$  of proton-proton collisions at a center-of-mass energy of 8 TeV. The analysis focusses on the decay of neutral Higgs bosons into a pair of tau leptons, which subsequently decay to an electron, a muon and four neutrinos. Furthermore, two channels are employed by requiring the presence or absence of a b-tagged jet, increasing sensitivity to the b-associated and gluon-gluon fusion production modes, respectively. Data driven methods are used to estimate  $Z \rightarrow \tau\tau$  and QCD multi-jet backgrounds. A reasonable agreement between the background estimations and the data is seen at preselection level. ....Something on exclusion limits....

Figure 2.19: Limits on the production of a scalar particle decaying to a di-tau pair and produced in association with b quarks (left) or via gluon-gluon fusion (right).





# Bibliography

- [1] L. Evans and P. Bryant, *LHC Machine*, JINST **3** (2008) S08001.
- [2] F. Englert and R. Brout, *Broken Symmetry and the Mass of Gauge Vector Mesons*, Phys. Rev. Lett. **13** (1964) 321.
- [3] P. W. Higgs, *Broken symmetries, massless particles and gauge fields*, Phys. Lett. **12** (1964) 132.
- [4] P. W. Higgs, *Broken Symmetries and the Masses of Gauge Bosons*, Phys. Rev. Lett. **13** (1964) 508.
- [5] P. W. Higgs, *Spontaneous Symmetry Breakdown without Massless Bosons*, Phys. Rev. **145** (1966) 1156.
- [6] G. S. Guralnik, C.R. Hagen and T. W. B. Kibble Phys.Rev.Lett. **13** (1964) 585.
- [7] N. P. Nilles, *Supersymmetry, supergravity and particle physics*, Phys. Rep. **110** (1984) 1.
- [8] H. E. Haber and G. L. Kane, *The search for supersymmetry: Probing physics beyond the standard model*, Phys. Rep. **117** (1985) 75.
- [9] ALEPH, DELPHI, L3 and OPAL Collaboration, *Search for neutral MSSM Higgs bosons at LEP*, Eur. Phys. J. **C47** (2006) 547.
- [10] *Combined CDF and D0 upper limits on MSSM Higgs boson production in tau-tau final states with up to  $2.2 \text{ fb}^{-1}$  of data*, arXiv:1003.3363 [hep-ex].
- [11] CDF Collaboration, T. Aaltonen et al. Phys. Rev. Lett. **103** (2009) 201801.
- [12] D0 Collaboration, V. Abazov et al. Phys. Rev. Lett. **101** (2008) 071804.
- [13] TNPWG (Tevatron New Physics Higgs Working Group), CDF and D0 Collaborations, *Search for Neutral Higgs Bosons in Events with Multiple Bottom Quarks at the Tevatron*, arXiv:1207.2757 [hep-ex].
- [14] CDF Collaboration, T. Aaltonen et al., *Search for Higgs Bosons Produced in Association with b-quarks*, Phys.Rev. **D85** (2012) 032005, arXiv:1106.4782 [hep-ex].

- [15] D0 Collaboration, V.M. Abazov et al., *Search for neutral Higgs bosons in the multi-b-jet topology in  $5.2\text{fb}^{-1}$  of  $p\bar{p}$  collisions at  $\sqrt{s} = 1.96\text{ TeV}$* , Phys.Lett. **B698** (2011) 97–104, [arXiv:1011.1931](#) [hep-ex].
- [16] The CMS Collaboration, S. Chatrchyan et al., [arXiv:1104.1619](#) [hep-ex] [hep-ex].
- [17] The ATLAS Collaboration, *Search for the neutral Higgs bosons of the Minimal Supersymmetric Standard Model in  $pp$  collisions at  $\sqrt{s} = 7\text{ TeV}$  with the ATLAS detector*, [arXiv:1211.6956](#) [hep-ex].
- [18] T. A. Collaboration, *Observation of a new particle in the search for the Standard Model Higgs boson with the ATLAS detector at the LHC*, Physics Letters B **716** (2012) 1–29.
- [19] T. C. Collatoration, *Observation of a new boson at a mass of  $125\text{ GeV}$  with the CMS experiment at the LHC*, Physics Letters B **716** (2012) 30–61.
- [20] S. Heinemeyer, O. Stål and G. Weiglein, *Interpreting the LHC Higgs search results in the MSSM*, Phys.Lett. **B710** (2012) 201–206, [arXiv:1112.3026](#) [hep-ph].
- [21] A. Arbey, M. Battaglia, A. Djouadi and F. Mahmoudi, *The Higgs sector of the phenomenological MSSM in the light of the Higgs boson discovery*, JHEP **1209** (2012) 107, [arXiv:1207.1348](#) [hep-ph].
- [22] The ATLAS Collaboration, G. Aad et al., *The ATLAS Experiment at the CERN Large Hadron Collider*, JINST **3** (2008) S08003.
- [23] M. L. Mangano et al., *ALPGEN, a generator for hard multiparton processes in hadronic collisions*, JHEP **07** (2003) 001.
- [24] J. Alwall et al., *Comparative study of various algorithms for the merging of parton showers and matrix elements in hadronic collisions*, Eur. Phys. J. **C53** (2008) 473, [arXiv:0706.2569](#).
- [25] S. Frixione and B. R. Webber, *Matching NLO QCD computations and parton shower simulations*, JHEP **06** (2002) 029, [hep-ph/0204244](#).
- [26] B. P. Kersevan and E. Richter-Was, *The Monte Carlo Event Generator AcerMC 2.0 with Interfaces to PYTHIA 6.2 and HERWIG 6.5*, [arXiv:0405247v1](#) [hep-ph].
- [27] G. Corcella et al., *HERWIG 6: an event generator for hadron emission reactions with interfering gluons (including supersymmetric processes)*, JHEP **01** (2001) 010.
- [28] J. M. Butterworth, J. R. Forshaw, and M. H. Seymour, *Multiparton Interactions in Photoproduction at HERA*, Z. Phys. **C72** (1996) 637.

- [29] T. Binoth, M. Ciccolini, N. Kauer, and M. Kramer, *Gluon-induced W-boson pair production at the LHC*, JHEP **12** (2006) 046.
- [30] A. S. et al., *Higgs boson production in gluon fusion*, JHEP **02** (2009) 029.
- [31] T. Gleisberg et al., *Event generation with SHERPA 1.1*, JHEP **02** (2009) 007.
- [32] J. Pumplin, D. R. Stump, J. Huston, H. L. Lai, P. M. Nadolsky and W. K. Tung, “New generation of parton distributions with uncertainties from global QCD analysis,” JHEP **0207** (2002) 012 [hep-ph/0201195].
- [33] H. -L. Lai, M. Guzzi, J. Huston, Z. Li, P. M. Nadolsky, J. Pumplin and C. - P. Yuan, “New parton distributions for collider physics,” Phys. Rev. D **82** (2010) 074024 [arXiv:1007.2241 [hep-ph]].
- [34] M. Carena, S. Heinemeyer, C. E. M. Wagner, and G. Weiglein, *Suggestions for benchmark scenarios for MSSM Higgs boson searches at hadron colliders*, Eur. Phys. J. **C26** (2003) 601–607, hep-ph/0202167.
- [35] The ATLAS Collaboration, *ATLAS Monte Carlo Tunes for MC09*, ATL-PHYS-PUB-2010-002.
- [36] S. Jadach, J. H. Kuhn and Z. Was, *TAUOLA - a library of Monte Carlo programs to simulate decays of polarized  $\tau$  leptons*, Comput. Phys. Commun. **64** (1990) 275.
- [37] E. Barberio, B. V. Eijk and Z. Was, *Photos - a universal Monte Carlo for QED radiative corrections in decays*, Comput. Phys. Commun. **66** (1991) 115.
- [38] The GEANT4 Collaboration, S. Agostinelli et al., *GEANT4 - a simulation toolkit*, Nucl. Instrum. Meth. **A506** (2003) 250.
- [39] The ATLAS Collaboration, G. Aad et al., *The ATLAS Simulation Infrastructure*, ATLAS-SOFT-2010-01-004, submitted to Eur. Phys. J. C., arXiv:1005.4568.
- [40] The ATLAS Collaboration, *Estimation of  $Z \rightarrow \tau\tau$  Background in VBF  $H \rightarrow \tau\tau$  Searches from  $Z \rightarrow \mu\mu$  Data using an Embedding Technique*, ATL-PHYS-INT-2009-109.
- [41] The ATLAS Collaboration, *Search for the Standard Model Higgs boson in the  $H \rightarrow \tau\tau$  decay mode with 4.7 fb of ATLAS detector*, Tech. Rep. ATLAS-CONF-2012-014, CERN, Geneva, Mar, 2012.
- [42] The ATLAS Collaboration, *Search for the Standard Model Higgs boson  $H \rightarrow \tau\tau$  decays with the ATLAS detector*, ATL-COM-PHYS-2013-722.
- [43] T. S. et al., *Z physics at LEP 1*, CERN 89-08 **3** (1989) 143.
- [44] The ATLAS Collaboration, *Expected Performance of the ATLAS Experiment - Detector, Trigger and Physics*, CERN-OPEN-2008-020, arXiv:0901.0512.

- [45] The ATLAS Collaboration, *ATLAS Muon Momentum Resolution in the First Pass Reconstruction of the 2010 p-p Collision Data at  $\sqrt{s} = 7$  TeV*, ATLAS-CONF-2011-046.
- [46] The ATLAS Collaboration, *Muon reconstruction efficiency in reprocessed 2010 LHC p-p collision data recorded with the ATLAS detector*, ATLAS-CONF-2011-063.
- [47] The ATLAS Collaboration, *Expected electron performance in the ATLAS experiment*, ATLAS-PUB-2011-006.
- [48] ATLAS egamma WG, *Electron efficiency measurements*, <https://twiki.cern.ch/twiki/bin/view/AtlasProtected/EfficiencyMeasurements>.
- [49] M. Cacciari, G. P. Salam, and G. Soyez, *The anti- $k_t$  jet clustering algorithm*, JHEP **04** (2008) 063.
- [50] W. Lampl et al., *Calorimeter Clustering Algorithms : Description and Performance*, ATL-LARG-PUB-2008-002.
- [51] T. Barillari et al., *Local Hadron Calibration*, ATL-LARG-PUB-2009-001.
- [52] The ATLAS Collaboration, *Jet energy scale and its systematic uncertainty in proton-proton collisions at  $\sqrt{s} = 7$  TeV in ATLAS 2010 data*, ATLAS-CONF-2011-032.
- [53] The ATLAS Collaboration, *Performance of the Reconstruction and Identification of Hadronic tau Decays in ATLAS with 2011 Data*, ATLAS-CONF-2012-142.
- [54] The ATLAS Collaboration, *Reconstruction and Calibration of Missing Transverse Energy and Performance in Z and W events in ATLAS Proton-Proton Collisions at  $\sqrt{s}=7$  TeV*, ATLAS-CONF-2011-080.
- [55] A. Elagin, P. Murat, A. Pranko, and A. Safonov, *A New Mass Reconstruction Technique for Resonances Decaying to di-tau*, arXiv:1012.4686 [hep-ex]. \* Temporary entry \*.
- [56] ATLAS Jet/EtMiss Combined Performance Group, *Jet Energy Resolution Provider*, <https://twiki.cern.ch/twiki/bin/view/Main/JetEnergyResolutionProvider>.
- [57] The ATLAS Collaboration, *Data-Quality Requirements and Event Cleaning for Jets and Missing Transverse Energy Reconstruction with the ATLAS Detector in Proton-Proton Collisions at a Center-of-Mass Energy of  $\sqrt{s} = 7$  TeV*, ATLAS-CONF-2010-038.
- [58] T. A. Collaboration, *Search for neutral MSSM Higgs bosons decaying to  $\tau\tau$  pairs in proton-proton collisions at with the ATLAS detector*, Physics Letters B **705** (2011) no. 3, 174 – 192.

- [59] The ATLAS Collaboration, *Data-driven estimation of the background to charged Higgs boson searches using hadronically-decaying tau final states in ATLAS*, ATLAS-CONF-2011-051.
- [60] The ATLAS Collaboration, *Measurement of the  $Z \rightarrow \tau\tau$  cross section with the ATLAS detector*, Phys. Rev. D **84** (2011) 112006.
- [61] T. A. Collaboration, *Search for the neutral Higgs bosons of the Minimal Supersymmetric Standard Model in  $pp$  collisions at  $\sqrt{s} = 7$  TeV with the ATLAS detector*, JHEP , [arXiv:1211.6956](#).
- [62] Atlas statistics forum, *ABCD method in searches*, [link](#)
- [63] The ATLAS Collaboration, *Search for Neutral MSSM Higgs Bosons  $H$  to  $\tau\tau$  to  $t\tau_h$  with the ATLAS Detector in 7 TeV Collisions*, ATL-COM-PHYS-2012-094.
- [64] The ATLAS Collaboration, *Search for neutral Higgs Bosons in the decay mode  $H \rightarrow \tau\tau \rightarrow ll+4\nu$  in proton proton collision at  $\sqrt{7}$  TeV with the ATLAS Detector*, ATL-COM-PHYS-2011-758.
- [65] The ATLAS Collaboration, *Measurement of the  $b$ -tag Efficiency in a Sample of Jets Containing Muons with  $5\text{ fb}^{-1}$  of Data from the ATLAS Detector*, ATLAS-CONF-2012-043.
- [66] The ATLAS Collaboration, *Luminosity Determination in  $pp$  Collisions at  $\sqrt{s} = 7$  TeV using the ATLAS Detector in 2011*, ATLAS-CONF-2011-116.
- [67] T. Sjostrand, S. Mrenna and P. Skands, *PYTHIA 6.4 physics and manual*, JHEP **05** (2006) 026.
- [68] A. B. et al., *Rivet user manual*, [arXiv:1003.0694](#) [hep-ph].
- [69] E. G. G. Cowan, K. Cranmer and O. Vitells, *Asymptotic formulae for likelihood-based tests of new physics*, [arXiv:1007.1727](#) [hep-ex].
- [70] LHC Higgs Cross Section Working Group, S. Dittmaier, C. Mariotti, G. Passarino, R. Tanaka (Eds.), et al., *Handbook of LHC Higgs Cross Sections: 1. Inclusive Observables*, [arXiv:1101.0593](#) [hep-ph].
- [71] LHC Higgs Cross Section Working Group, S. Dittmaier, C. Mariotti, G. Passarino, and R. Tanaka (Eds.), *Handbook of LHC Higgs Cross Sections: 2. Differential Distributions*, CERN-2012-002 (CERN, Geneva, 2012) , [arXiv:1201.3084](#) [hep-ph].
- [72] D. de Florian, G. Ferrera, M. Grazzini and D. Tommasini, *Transverse-momentum resummation: Higgs boson production at the Tevatron and the LHC*, JHEP **1111** (2011) , [arXiv:1109.2109](#) [hep-ph].
- [73] Statistical twiki, NuisanceCheck. <https://twiki.cern.ch/twiki/bin/view/AtlasProtected/NuisanceCheck>

## .1 Object Reconstruction, Preselection and Efficiency Corrections

In this section the preselection and reconstruction criteria for the objects used in this analysis are presented. For each object and selection criteria all corrections that have been applied to data and MC are also described. A summary of the preselection on physics objects used in this analysis is reported in Table 12.

### .1.1 Electrons

This analysis uses electrons found by the standard electron identification algorithms [44] that pass the **Medium++** criteria. A preselection is applied to the electrons to ensure that the electron cluster has a transverse energy of  $E_T > 15\text{GeV}$ , is within the pseudorapidity range  $|\eta| < 2.47$ , but is outside of the region  $1.37 < |\eta| < 1.52$ . The first requirement ensures that the selected electrons are within a range of  $E_T$  where the electron reconstruction and trigger efficiencies are well understood. The further requirements ensure that the electron is reconstructed within the acceptance of the ATLAS tracking, but outside of the transition region between the barrel and end-cap calorimeters. In addition, the electron is required to be either one or three, to ensure that the electron was reconstructed with either the standard electron algorithm or both the standard and soft electron algorithms, respectively. Finally, to ensure that the electron is not reconstructed within a region of the calorimeter with readout problems, dead or non-nominal high voltage conditions or suffering from high noise, the electron is rejected if the cluster  $\eta$  and  $\phi$  position match a flagged region in the Object Quality maps (OQ maps) [?] provided by the egamma Performance group.

For the electrons used in this analysis, the four-vector of the particle is defined using the energy of the electron calorimeter cluster and the direction of the electron track. Selections that involve the electron position in the calorimeter, in this analysis the  $\eta$  and the OQ map selections, are made using a four-vector built entirely from the electron cluster properties. Both the energy scale and resolution of the electrons used in this analysis are corrected, following the recommendations of the EGamma performance group, by using the `egammaAnalysisUtils` package[?]. Energy scale corrections are applied to electrons in data, whereas an additional smearing is applied to the electron energy in MC.

In addition to the preselection defined above, isolation criteria are defined to select electrons with little or no activity around them. The calorimetric isolation,  $E_T(\text{cone})$ , is calculated as the sum of the transverse energy of the additional topological clusters in the electromagnetic and hadronic calorimeters in a cone of  $\Delta R < 0.2$  around an electron<sup>3</sup>. The summed transverse energy is corrected, as a function of the number of primary vertices in the event, to reduce the dependence on pileup. In addition, the track isolation,  $p_T(\text{cone})$ , is defined as the scalar sum of the  $p_t$  of all additional tracks with  $p_t > 1\text{ GeV}$  in a cone of radius  $\Delta R < 0.4$

---

<sup>3</sup>The  $\Delta R$  variable is defined by  $\Delta R = \sqrt{(\Delta\eta)^2 + (\Delta\phi)^2}$ , where  $\Delta\eta$  and  $\Delta\phi$  correspond to the difference between the pseudorapidities and azimuthal angles of the objects considered, respectively.

around an electron. In this analysis, an electron with  $E_T(\text{cone})/p_t < 0.08$  and  $p_T(\text{cone})/p_t < 0.06$  is considered isolated.

## .1.2 Muons

Muons reconstructed by the STACO algorithm [44] are used in this analysis - those passing the STACO Loose quality criteria are considered at the preselection stage, whereas the more stringent STACO Combined quality criteria are required for the final muon selection. Muons with a transverse momentum  $p_t > 10$  GeV and within the pseudorapidity range  $|\eta| < 2.5$  are selected. The difference between the  $z$  position of the muon track extrapolated to the beam line and the primary vertex  $z$  position must be less than 10 mm.

Further quality criteria are placed on the Inner Detector track of the muon candidate to ensure that it is well reconstructed and to reduce the fake rate due to decays of hadrons in flight. These requirements ensure that multiple hits are found on the track in the various layers of the ID, but take into account that dead or uninstrumented regions may be crossed by the muon. Firstly, if the muon passes through a section of the b layer of the Pixel detector that is instrumented and not suffering from detector problems, there should be one or more b layer hits on the track. The sum of the number of hits on the track in the Pixel detector and the number of crossed dead Pixel detector layers should be at least one. The sum of the number of hits within the SCT detector and the number of dead SCT modules crossed should be five or greater. The total number of crossed dead Pixel detector and SCT detector layers should be less than three. When within the angular region  $|\eta| < 1.9$ , the sum of the TRT hits and outliers on the track must be greater than five and the ratio of TRT outlier hits to the total number of TRT hits must be less than 0.9. When the muon track is in the region  $|\eta| \geq 1.9$ , the ratio of TRT outlier hits to the total number of TRT hits must be less than 0.9 only if the sum of the TRT hits and outliers on the track is greater than five.

The momentum scale and resolution of the muons in this analysis are corrected in MC following the recommendations of the Muon Combined Performance group. The momentum corrections were measured by comparing the di-muon mass peak position and resolution between data and MC at the Z resonance. Smearings are applied in a coherent manner to the ID, MS extrapolated and combined momenta of the transverse momentum of the muon. In addition, a scale correction is applied to the combined momentum momentum.

As for the electrons used in this analysis, both calorimetric and track based isolation are used to require little or no activity around them, in addition to the preselection above. The muon  $E_T(\text{cone})$  and  $p_T(\text{cone})$  variables are defined as for the electron case and are calculated in cones of  $\Delta R < 0.2$  and  $\Delta R < 0.4$  around the muon, respectively. Once more  $E_T(\text{cone})$  is corrected as a function of the number of primary vertices in the event, to reduce the dependence on pileup. In this analysis, a muon with  $E_T(\text{cone})/p_t < 0.04$  and  $p_T(\text{cone})/p_t < 0.06$  is considered isolated.

### .1.3 Jets

The jets used in this analysis are reconstructed using the Anti- $k_T$  algorithm [49] with the distance parameter  $R=0.4$  taking topological clusters as inputs. The reconstructed jets are calibrated to the Local Cluster Weighting (LCW) scale [?]. In addition, the effect of pileup on the reconstructed energy is reduced by applying a further correction based on the pile-up area method with a final in-situ calibration also applied.

A preselection is then applied that requires the reconstructed jets have a transverse momentum, after calibration, of  $p_t > 30$  GeV and to be within the pseudorapidity range  $|\eta| < 4.5$ . The effect of pileup on the reconstructed jets is further reduced by requiring that jets with the pseudorapidity range  $|\eta| < 2.4$  and a transverse momentum of  $p_t < 50$  GeV have a absolute value of the Jet Vertex Fraction (JVF) of greater than 0.5.

A separate set of preselected jets is defined that are used only for b-tagging (henceforth known as “taggable jets”). Such jets are reconstructed and calibrated as for the standard preselected jets. However, the taggable jets are required to have a transverse momentum of  $p_t > 20$  GeV and to have a reconstructed pseudorapidity of  $|\eta| < 2.5$ . The second requirement ensures that charged particles within the jets pass through the tracking volume and hence can be used for b-tagging of the jet. Finally, the same JVF selection as the standard preselected jets is applied to the taggable jets.

### .1.4 b-Tagging

The tagging of jets due to the hadronisation of b-quarks is performed using the MV1 b-tagging algorithm [?]. This neural network based algorithm uses the output weights of the JetFitter+IP3D, IP3D and SV1 b-taggers as inputs. The working point that gives a nominal b-tagging efficiency of 70% on  $t\bar{t}$  samples is used.

### .1.5 Taus

Hadronically decaying tau candidates are reconstructed using clusters in both the electromagnetic and hadronic calorimeters. A preselection is applied to the candidates that requires the reconstructed  $\tau$  candidates to have a transverse momentum of  $p_t > 20$  GeV and to have a reconstructed pseudorapidity of  $|\eta| < 2.5$ . Furthermore, it is required that the candidates have either one or three tracks within a cone of  $\Delta R < 0.2$  associated to them and have a charge of  $\pm 1$ . Finally, the preselected tau candidates should pass the BDT-Medium multivariant tau identification selection as well as the dedicated electron and muon vetoes for hadronically decaying tau candidates.

### .1.6 Overlap Removal

After the preselection of the physics objects needed for this analysis, an overlap removal between the different objects is then applied to avoid double-counting.



The distance between two objects in rapidity  $\Delta\eta$  and polar angle  $\Delta\phi$  is defined as  $\Delta R = \sqrt{(\Delta\eta)^2 + (\Delta\phi)^2}$ . Overlap removal is then applied in the following order:

- preselected electrons are removed if they overlap with a preselected muon within  $\Delta R < 0.2$ ,
- preselected taus are removed if they overlap with a preselected muon or electron within  $\Delta R < 0.2$ ,
- preselected jets are removed if they overlap with a preselected muon, electron or tau within  $\Delta R < 0.2$ .

### .1.7 Missing Transverse Energy

The missing transverse energy,  $E_T^{miss}$ , is calculated using the RefFinal method, which takes the energy deposited in the calorimeter, the muons reconstructed in the muon spectrometer and tracks reconstructed in the inner detector as inputs. For this, the energy deposits are calibrated based upon the high- $p_t$  physics object they are associated to, with an order of preference of electrons, photons, hadronically decaying taus, jets and finally muons. Any unassociated energy deposits are combined into the so-called “soft-term”. To reduce the effect of pileup on the  $E_T^{miss}$  calculation, corrections are applied to both the jets in an event and to the soft-term. Firstly, any jet with a pseudorapidity of  $|\eta| < 2.4$  that enters the  $E_T^{miss}$  calculation is weighted by its JVF. Similarly, the soft-term is weighted by the soft-term-vertex-fraction (STVF) of the event - the ratio given by

$$STVF = \frac{\sum_{track,PV} p_t}{\sum_{track} p_t} \quad (3)$$

where  $\sum_{track,PV} p_t$  is the sum of the transverse momentum of all tracks associated to the primary vertex, but unmatched to physics objects, and  $\sum_{track} p_t$  is the sum of the transverse momentum of all tracks in the event unmatched to physics objects. Any calibration applied to the energy or direction of the physics objects in the final analysis is also propagated to the  $E_T^{miss}$ .

### .1.8 Vertices

In this analysis vertices are selected that have a minimum of three associated tracks: this helps to ensure that the selected vertices come from beam-beam interactions rather than, for instance, cosmic muons.

### .1.9 Event Cleaning

In addition to the data quality requirements described in section ??, further selections are applied to veto events where bad jets are identified as arising from detector effects (coherent noise in the EM and Tile calorimeters or spikes in the

Physics Object	Preselection
Electrons	$p_t > 15 \text{ GeV}$ $ \eta  < 1.37 \text{ or } 1.52 <  \eta  < 2.47$ <b>Medium++</b> Author = 1 or 3 Pass Object Quality Flag
Muons	$p_t > 10 \text{ GeV}$ $ \eta  < 2.5$ isLoose STACO muon Inner Detector track quality requirements Inner Detector track $ z_0^{PV}  < 10\text{mm}$
Jets	$p_t > 30 \text{ GeV}$ $ \eta  < 4.5$ $ JVF  > 0.5$ for jets with $ \eta  < 2.4$ and $p_t < 50 \text{ GeV}$
Jets (taggable)	$p_t > 20 \text{ GeV}$ $ \eta  < 2.5$ $ JVF  > 0.5$ for jets with $ \eta  < 2.4$ and $p_t < 50 \text{ GeV}$
Taus	$p_t > 20 \text{ GeV}$ $ \eta  < 2.5$ BDT Medium $N_{tracks} = 1\text{or}3$ Author = 1 or 3 Muon and Electron Veto
$E_T^{miss}$	RefFinal with STVF correction
Vertices	$N_{tracks} \geq 3$

Table 12: Summary of the preselections used for physics objects in this analysis

HEC calorimeter), cosmics or beam based background. To reject events, the recommendations of the JetEtMiss performance group [?] are followed: Events are rejected if at least one AntiKt4LCTopo jet with  $p_T > 20 \text{ GeV}$ , that passes the overlap removal with electrons, muons and taus described in section .1.6, fails the **BadLooseMinus** selection or points towards the hot Tile Calorimeter cells identified in data taking periods B1 and B2 [?].

## .1.10 Monte Carlo Corrections

The MC samples used on this analysis are corrected to account for differences between the simulation and data in the trigger, lepton reconstruction and identification and b-tagging efficiencies. Furthermore, the MC is reweighted so that the vertex multiplicity distribution agrees with that in the data.

### Trigger Efficiency corrections

Correction factors are applied to the simulated trigger efficiency for both the single electron,

EF\_e24vhi\_medium1, and combined electron-muon, EF\_e12Tvh\_medium1\_mu8, triggers used in this analysis. The trigger efficiency for the EF\_e24vhi\_medium1 has been measured with respect to offline electrons using a tag and probe method in  $Z \rightarrow ee$  events [?]. Scale factors are derived from the ratio of the trigger efficiency measured in data and MC, measured as a function of electron  $p_t$  and  $\eta$ .

For the EF\_e12Tvh\_medium1\_mu8 trigger, correction factors are measured separately for the two individual legs of the trigger, EF\_e12Tvh\_medium1 and EF\_mu8 [?]. The product of the two correction factors is then used as the overall scaling factor. The trigger efficiency for the EF\_e12Tvh\_medium1 leg has been measured with respect to offline electrons using a tag and probe method for  $Z \rightarrow ee$  events in both data and MC. Likewise, the EF\_mu8 trigger efficiency scale factors are derived using a tag and probe measurement with  $Z \rightarrow \mu\mu$  events. Oncemore, scale factors are derived from the ratio of the trigger efficiency measured in data and MC, measured as a function of electron  $p_t$  and  $\eta$ .

### Lepton Reconstruction Efficiency Corrections

Further correction factors are applied to the MC samples to account for differences in the lepton reconstruction and identification efficiencies between data and simulation. Scale factors for the electron identification and reconstruction efficiencies are measured separately using a combination  $Z \rightarrow ee$  and  $J/\psi \rightarrow ee$  tag and probe measurements [?]. Both sets of scale factors are measured as a function of the electron  $E_T$  and  $\eta$ .

Similarly, muon reconstruction efficiency scale factors have been measured, using a  $Z \rightarrow \mu\mu$  tag and probe analysis, as a function of the muon  $p_t$ ,  $\eta$ ,  $\phi$  and charge [?].

### b-tagging Efficiency Corrections

Corrections are applied to the b-tagging efficiency and mistag rate in MC, using a combination of the System8 and likelihood scale factor measurements [?]. Separate scale factors are applied based on the origin of the jet at truth level - from a  $b$  quark, a  $c$  quark, a  $\tau$  or a light quark - and are applied as a function of the jet  $p_t$  and  $\eta$ .

### Pileup Reweighting

Differences between the distribution of the average number of interactions per bunch crossing,  $\langle \mu \rangle$ , in MC and data are corrected by reweighting the MC  $\langle \mu \rangle$  distribution to that in the full considered dataset. An additional scaling of  $1.1 \times \langle \mu \rangle$  is applied to the MC, which has been shown to improve the description of the number of primary vertices distribution of the data.